Synthesis, Structures and Properties of Thermoelectric Materials in the Zn-Sb-In System

by

Yang Wu

A Dissertation Presented in Partial Fulfillment
of the Requirements for the Degree
Doctor of Philosophy

Approved April 2011 by the
Graduate Supervisory Committee:

Ulrich Haussermann, Chair
Dong Seo
William Petuskey
Nathan Newman

ARIZONA STATE UNIVERSITY

May 2011

ABSTRACT

The challenging search for clean, reliable and environmentally friendly energy sources has fueled increased research in thermoelectric materials, which are capable of recovering waste heat. Among the state-of-the-art thermoelectric materials β-Zn_4Sb_3 is outstanding because of its ultra-low glass-like thermal conductivity. Attempts to explore ternary phases in the Zn-Sb-In system resulted in the discovery of the new intermetallic compounds, stable $Zn_5Sb_4In_{2-\delta}$ (δ=0.15) and metastable $Zn_9Sb_6In_2$. Millimeter-sized crystals were grown from molten metal fluxes, where indium metal was employed as a reactive flux medium. $Zn_5Sb_4In_{2-\delta}$ and $Zn_9Sb_6In_2$ crystallize in new structure types featuring complex framework and the presence of structural disorder (defects and split atomic positions). The structure and phase relations between ternary $Zn_5Sb_4In_{2-\delta}$, $Zn_9Sb_6In_2$ and binary Zn_4Sb_3 are discussed. To establish and understand structure-property relationships, thermoelectric properties measurements were carried out. The measurements suggested that $Zn_5Sb_4In_{2-\delta}$ and $Zn_9Sb_6In_2$ are narrow band gap semiconductors, similar to β-Zn_4Sb_3. Also, the peculiar low thermal conductivity of Zn_4Sb_3 (1 W/mK) is preserved. In the investigated temperature range 10 to 350 K $Zn_5Sb_4In_{2-\delta}$ displays higher thermoelectric figure of merits than Zn_4Sb_3, indicating a potential significance in thermoelectric applications. Finally, the glass-like thermal conductivities of binary and ternary antimonides with complex structures are compared and the mechanism behind their low thermal conductivities is briefly discussed.

ACKNOWLEDGMENTS

It is more than fortunate to have Dr. Ulrich Häussermann as the advisor for my Ph.D. study. I would like to gratefully and sincerely thank him for his instruction, patience, and most importantly his mentorship in my study. His knowledge, experience and kindness provide me invaluable help for my dissertation. I am not sure that how many students are encouraged to think independently but I feel very lucky that I am one of them. Ulrich, for everything you have done for me in the past six years, I need to say thank you, thank you for opening the door of solid state chemistry for me.

I deeply understand without any help and collaboration I can not make any achievements. I gratefully acknowledge all my committee members. Dr. Don Seo, Dr. Bill Petuskey and Dr. Nate Newman. Thank you for your insightful instructions and discussions in these years. I also would like to thank Dr. Tom Groy, for his expertise in the crystallography, Dr. Kurt Leinenweber, for his tremendous experience in multi-anvils and Dr. Javier Garcia for his help of TEM, as well as those wonderful dinners we have had together in Augsburg.

I also enjoy the time to work in a very international group because almost everybody is from different countries. Dr. Mike Evans, Dr. Toyoto Sato, Dr. Johanna Nylen, Dr, Andreas Tenga, Dr. Emil Stoyanov, Verina, Kati, and Sumit, thank you for the help and collaboration. The experience of working with you will be my precious memory. Particularly, Toyoto, wish you and your country the best of working out of the disaster.

Besides my group mates, I also thank ASU for providing me the opportunity of study, facilities and financial support. Many thanks to all my colleagues and friends that I worked with together at ASU. Dr. Sanghwan Kim, Dr. Qiangbin Wang, Dr. Chang'e Weng and Sanjita from Dr. Seo's group, Dr. Feng He from Dr. Petuskey's group and Dr. Yi Shen, Dr. Zhizhong Tang, Lei Zhang, Mengchu Huang and Lingtao Liu from Dr. Newman's group thank you for your kind helps and discussions for my experiments. Craig, thank you for the help from the aspect of high pressure experiments. Also, I thank all friends that we meet in the gym to enjoy basketball together.

I appreciate the opportunity for going to Germany and the experience with another culture. I sincerely thank Dr. Wolfgang Scherer's group for the host of my stay and education of charge density study of chemical bonding. Thanks to Dr. Georg Eickerling, Dr. Ernst-Wilhelm Scheidt, Christoph, Andreas and Mrs. Fischer, for their help.

Additionally, I would like to thank my family members for their endless help and understand. Thanks to my mother, father, grandpa, grandma and my wife, Hu shuna, your support is always my greatest motivation.

TABLE OF CONTENTS

Page

CHAPTER Page

Page

LIST OF TABLES

TABLE Page

LIST OF FIGURES

FIGURE Page

FIGURE Page

Chapter 1

INTRODUCTION TO THERMOELECTRIC MATERIALS: SIGNIFICANCE AND STATE-OF-THE-ART

The development of world's economy requires sustainable energy sources along with a reduced emission of carbon dioxide. The most recent energy flow chart, developed at Lawrence Livermore National Laboratory (LLNL), illustrates the constituents of energy sources in the U.S. in 2009 (figure 1.1).[1] The major part of the energy consumed in the U.S. is from carbon-containing fossil fuels, i.e., coal, petroleum and natural gas. Nevertheless, none carbon-containing sources play an increasingly important role in the energy mix. According to LLNL, wind power increased drastically from 0.51 quadrillion British Thermal Units (quads) in 2008 to 0.70 quads in 2009. The continuous development of renewable energy sources, such as nuclear, solar, geothermal, biomass, hydro and wind power is commensurate with the reduction of carbon emission. In parallel to the concerted efforts to expand the range of energy sources, energy conversation becomes increasingly important. In 2009, the total amount of energy used in the U.S. is 94.6 quads, down from 99.2 quads in 2008.[1] The decrease could be accounted for by a wider adoption of more efficient electronic devices as well as declined economic activity. However, most striking is the fact that a big portion of the energy produced today is lost as heat (54.64 quads) and only less than half actually serves human society (39.97 quads). Therefore, for solving a potential future energy crisis, ways to recover waste energy (heat) should be included in the future energy landscape since even a small part of energy converted from waste

heat will have a significant impact.[2] In this respect, thermoelectric power generation represents one possibility.

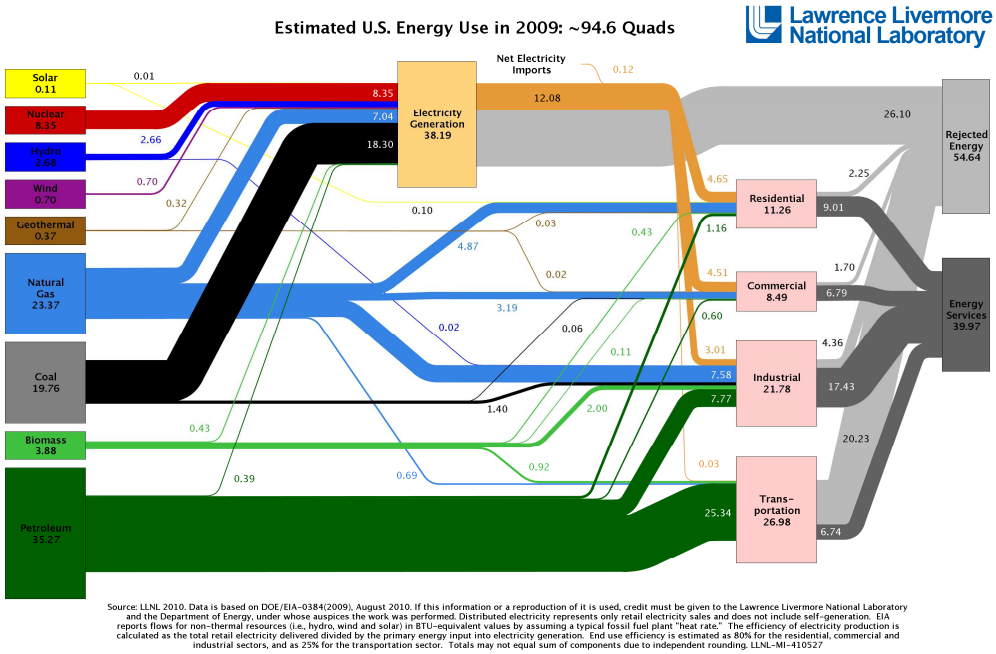

Figure 1.1. The Energy Use in USA in 2009.[1]

1.1 The Thermoelectric Effects

Thermoelectric materials provide a way of energy conversion between heat and electricity. Two thermoelectric effects have been known since 19th century: (i) power generation, discovered by Thomas Seebeck, and (ii) refrigeration, discovered by Jean Peltier. Until the 1950s', these effects draw only attentions as laboratory curiosities.[3] This changed recently when the potential significance of thermoelectric power generation for waste heat recovery was realized.[4,5,6,7,8,9]

Modern semiconductor theory provides insight into fundamental understanding of thermoelectric effect. Peltier effect occurs when a circuit (shown

in figure 1.2) composed of a pair of conductors, is subject to a current. Then one joint is heated while the other is cooled. Let us assume that this circuit contains an n-type semiconductor and a metal which are situated in a uniform temperature distribution. Without any electric field, the Fermi levels for the semiconductor and the metal will coincide and all mobile electrons should have the same energy. This scenario changes when a current flows through the junction. The applied electric field produces a discontinuity in the Fermi level across the junction. On the semiconductor side, the average energy of "moving" electrons, which should be electrons in the conduction band for an n-type semiconductor, is given by ΔE_t , which is the average energy of electrons in the conduction band with respect to the Fermi level. On the metal side, the average energy of "moving" electrons is denoted by ΔE_m, with respect to Fermi level. It is obvious that the difference ΔE_t is greater than ΔE_m. Therefore, when electrons transfer from the metal side to the semiconductor side, the amount of energy $(\Delta E_t - \Delta E_m)$ needs to be absorbed from surroundings. The same amount of energy will be released at the other junction as electrons transfer from the semiconductor to the metal. Hence, the Peltier coefficient is derived as

$$\Pi = (1/e)(\Delta E_t - \Delta E_m) \qquad (1.1)$$

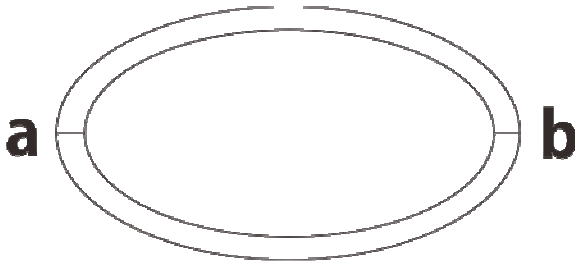

Figure 1.2. A circuit composed of two different conductors with joints a and b. Peltier effect, when a current passes through, joints a and b show different temperatures. Seebeck effect, when temperatures of a and b are different, a voltage drop will be observed in case the circuit is open.

If the temperature between joints a and b in figure 1.2 is different, a voltage will appear if either of a and b is opened. This phenomenon, called Seebeck effect, is exploited in thermocouples for temperature measurement.[10] The Seebeck voltage is produced by the fact that the density of charge carriers redistributes in a temperature gradient. Carriers with higher energy will diffuse toward the cold end and a net current appears. This current will cause an opposite voltage and the total current becomes zero. The voltage is proportional to temperature gradient and the ratio is defined as Seebeck coefficient, which for the circuit of figure 1.2 is,

$$\alpha_{ab} = \frac{V}{\Delta T} \qquad (1.2)$$

where V is the voltage and ΔT is the temperature gradient.

The Seebeck and Peltier effects share the same interpretation based on charge carrier diffusion. In 1857,[11] Lord Kelvin established a thermodynamic relationship between them which is

$$\Pi_{a,b} = \alpha_{a,b} T \qquad (1.3)$$

where T is the absolute temperature. Kelvin also proposed a third thermoelectric effect: Reversible heating or cooling occurs when a current passes through a conductor which at the same time is subjected to a temperature gradient. The theory established by Kelvin gives the basis of deriving the efficiency of thermoelectric energy conversion, on which the development of modern thermoelectric materials and devices is rooted.

1.2 The Efficiency of Thermoelectric Materials

Modules generated by pairing up an n-type conductor and a p-type conductor leg can be employed for both refrigeration and power generation (figure 1.3). Since there is no need of a compressor and chlorofluorocarbons coolants, thermoelectric refrigeration (figure 1.3, left) is very compact and environmental friendly. As discuss earlier, power generation based on Seebeck effect (figure 1.3, right) has potential in low level heat recovery, which can be used to improve the fuel efficiencies for automobile engines.[12] However, what limits the commercial practicality of thermoelectric devices is their low efficiencies. The primary barrier to improving thermoelectric devices is the thermoelectric materials themselves.

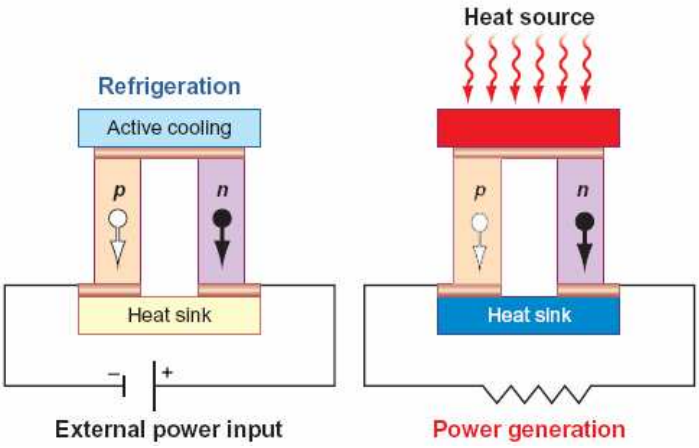

Figure 1.3. Schematic of thermoelectric refrigeration (left) power generation and power generation (right).[13]

The efficiency of a thermoelectric device, like all other engines, is defined as the output of the energy divided by the energy consumed, i.e.,

$$\eta = w / q \qquad (1.4)$$

Ioffe in 1957 derived that highest efficiency for power generation can be represented as[14,15]

$$\eta = \frac{(T_H - T_C)}{T_H} \frac{\sqrt{(1+ZT)}}{T_c / T_H + \sqrt{(1+ZT)}} \quad (1.5)$$

where T is the average temperature. The first term corresponds to Carnot efficiency, which becomes the highest limit of η since the second term is always less than 1. The quantity ZT, which is known as figure of merit, is given by

$$ZT = \frac{\alpha^2 \sigma}{\kappa} T \quad (1.6)$$

where α is Seebeck coefficient, σ is electrical conductivity, κ is total thermal conductivity and T is the average temperature ($T = (T_H + T_C)/2$). η will generally increase with *ZT*.

Accordingly, a good thermoelectric material must simultaneously possess a high Seebeck coefficient, a high electrical conductivity and a low thermal conductivity. These three factors are interrelated and make it quite challenging to optimize *ZT*. Equation 1.6 emphasizes that high Seebeck coefficients are important for a good thermoelectric material. Nevertheless, an increase in S is almost always accompanied with a decrease in σ. Typically semiconductors and semimetals have higher S but lower σ than metals because of their rather lower carrier concentrations. The thermal conductivity, κ, consists of two parts, a contribution from lattice vibration, κ_L, and a contribution from the charge carriers, κ_e. According to the Wiedemann-Franz law, any increase in carrier concentration will favorably increase σ but also (unfavorably) increase κ_e.[16]

It is necessary to identify a charge carrier range where the two trade-off factors S and σ can reach their maximum product of $S^2\sigma$ while κ_e stays reasonably low. Snyder, et al., suggested that the maximum *ZT* is achieved with carrier concentrations 10^{19} to10^{21} cm^{-3} (figure 1.4).[4] Today, most state-of-the-art thermoelectric materials are heavily doped semiconductors or semimetals with narrow band-gaps. It is noteworthy that in a semiconductor minority carriers are always thermally activated and will play a detrimental role to the Seebeck coefficient. It has been suggested that for a good thermoelectric material the band gap should be around 10 k_BT ("10 k_BT rule").[17]

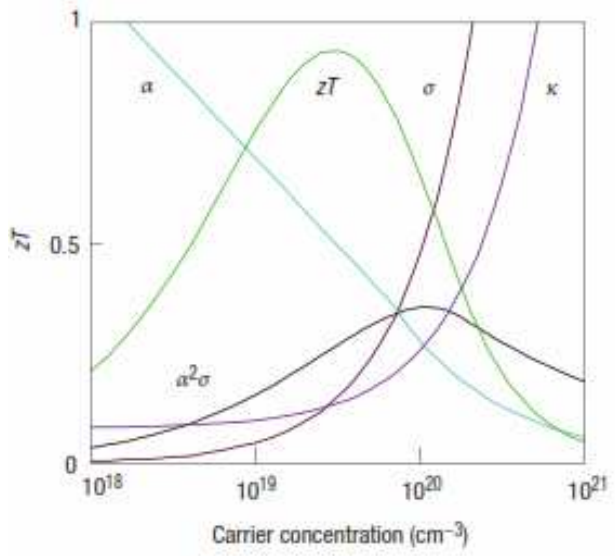

Figure 1.4. Curves showing *ZT* as a function of carrier concentration.[4]

Apart from possessing the optimum carrier concentration, the lattice thermal conductivity κ_L of a thermoelectric material needs to be as low as possible. Lowest thermal conductivity is found for glasses,[18] where thermal conduction is carried out by random walks of vibrations instead of lattice phonons. However, glasses are poor electrical conductors and, thus, cannot reach high power factors $S^2\sigma$. To describe this dilemma, Slack proposed the expression "phonon glass electron crystal" for ideal thermoelectrics.[19] "Electron crystal" refers to the requirement that materials should meet the ideal compromise of S, σ, and κ_e, i.e. the properties governed by electrons, and "phonon glass" reflects the requirement that the lattice thermal conductivity should be as low as possible.

1.3 State-of-the-Art Thermoelectric Materials

Figure 1.5 displays a compilation of state-of-the-art thermoelectric materials (ZT > 1). Some of them will be described briefly in the following.

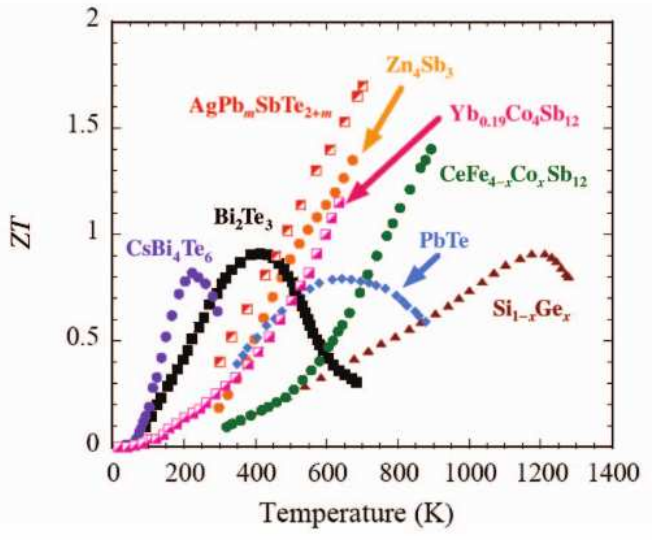

Figure 1.5. *ZT* as a function of temperature for some of bulk thermoelectric materials, complied by Tritt, T. M. and Subramanian, M. A..[20]

Bismuth Tellurides

One of the most useful thermoelectric materials today is Bi_2Te_3 and its alloys with antimony telluride or bismuth selenide. Bi_2Te_3 crystallizes in a rhombohedral structure with layers formed by Bi and Te atoms. These layers follow the sequence Te-Bi-Te-Bi-Te. Atoms within this sequence are strongly connected by covalent Bi-Te bonding while between sequences there are only weak van der Waals interactions. Accordingly, this material is easily cleaved perpendicular to the c-axis and its properties are highly anisotropic.

Bi_2Te_3 displays a small energy gap of around 0.15eV and a Seebeck coefficient close to $\pm 200\mu V/K$.[21] According to the "10 k_BT rule" discussed in the early section, Bi_2Te_3 offers the best thermoelectric performance below or about room temperature which renders its application primarily to thermoelectric

cooling. By alloying with Sb or Se or both, κ_L is substantially reduced (from 1.4 W/mK to 0.6 W/mK at room temperature).[22]

Variations of the Bi_2Te_3 structural theme can be achieved by introducing electropositive alkali metals. Electropositive metals act as electron donors to the layer building blocks, which rearrange and form additional bonds. Remarkably complex compositions and structures result. Among them the chalcogenides $K_2Bi_8S_{13}$ and $K_{2.5}Bi_{8.5}Se_{14}$ have been shown promising thermoelectric properties, especially through a low thermal conductivity.[23,24,25] The highlight, however, is $CsBi_4Te_6$ which was reported by Chung, et al.[26] This new material has a similar electronic structure as Bi_2Te_3 and reaches a maximum *ZT* of 0.8 at 225K when optimally doped, making it an outstand candidate for low temperature applications.

Skutterudites

Skutterudites are binary compounds with the general formula MX_3 where M is group 9 transition metals and X is a heavier pnictogen element (P, As, Sb). Binary skutterudites crystallize in the body centered cubic space group *Im*3. The structure corresponds to a three-dimensional array of corner connected MX_6 octahedra which are mutually tilted (figure 1.6). It is noteworthy that because of the tilting, pnictogens atoms approach and thus form planar rectangular rings, which is also shown in figure 1.6. A second consequence of the tilted octahedra is the creation of voids at the unit cell corners and center (position 2*a* (0,0,0)). Skutterudites reveal diamagnetic and semiconducting behavior. The major bonding interaction is between the transition metal and pnictogen atoms. The band gaps is a

consequence of the strong interaction between d and p states (dp hybridization gap). The completely filled valence band hosts 18 electrons.

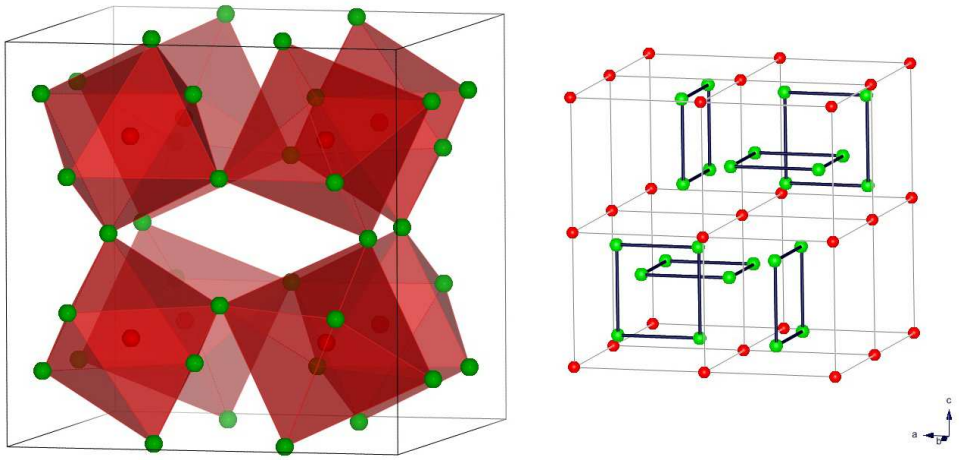

Figure 1.6 The structure of a skutterudite, $CoSb_3$. Red atoms are Co and green atoms are Sb. Left, arrangement of corner-connected $CoSb_6$ octahedra in a unit cell. Right, the unit cell has been shifted along the body diagonal by illustrate the presence of rectangular antimony rings.

The thermal conductivity for binary skutterudites is rather high and they haven't been considered as promising thermoelectric materials until ternary derivatives were found where voids are partially occupied with guest atoms. The synthesis of filled skutterudites has been pioneered by Jeitschko and his co-workers.[27,28] Guest atoms are typically rare earth metal atoms, such as La, Ce and Yb, which allow for a tuning of the doping level towards optimum carrier concentrations.[29] With larger amounts of guest atoms an exchange of Co for more electron poor Fe becomes possible, and filled skutterudites can be p- and n-type conductors. Guest atoms are loosely bonded in the voids and will scatter lattice phonons by their thermal motion. This rattling effect of void-filling atom is

usually associated with the dramatic decrease in thermal conductivity,[30,31] even though the mechanism is still elusive. There have been several examples for filled skutterudites, such as $CeFeSb_3$, $CeFeAs_3$, $CeFe_{4-x}Co_xSb_{12}$, $LaFe_{4-x}Co_xSb_{12}$ ($0<x<4$), which display a ZT around 1 at elevated temperatures.[32,33,34,35]

Clathrates

Similar to skutterudites clathrates possess a framework with voids (or rather cages) that enclose guest atoms. The framework of clathrates is formed by group 14 element (Si, Ge, Sn) atoms that are tetrahedrally coordinated. Therefore, as for skutterudites the framework structure of clathrates is electron precise. On the other hand, clathrates frameworks are not stable without guest atoms, typically corresponding to formally electron donating alkali and alkaline earth metals. The presence of "guest" atoms has various consequences. Binary clathrates are usually n-type conductors. However, the framework structure may balance excess electrons by introducing vacancies and by this reinstall the electron precise, semiconducting, situation. Secondly, the framework may be composed of two types of atoms, tetravalent group 14 and trivalent group 13 ones (Al, Ga, In). In ternary clathrates excess electrons from guest atoms can be balanced by the presence of group 13 atoms in the framework.

Clathrates display very interesting thermoelectric properties. Prominent is a low thermal conductivity which is very similar to glasses. A theoretical study showed that the systems, $Sr_8Ga_{16}Ge_{30}$, $Ba_8Ga_{16}Si_{30}$, and $Ba_8In_{16}Sn_{30}$ are semiconductors, which by appropriate n- or p-doping can reach a *ZT* of 0.5 at room temperature, and values as high as 1.7 at 800 K.[36] Property measurements

have shown rather varied *ZT* values.[37,38] The best thermoelectric clathrate currently known is $Ba_8Ga_{16}Ge_{30}$ with a figure of merit of 1.35 at 900K.[39]

The concentration of guest atoms and/or the ratio of tri- and tetravalent framework atoms in ternary clathrates provide a means of tuning the electron transport properties. Similar to skutterudites, the low thermal conductivity of clathrates is attributed to a "rattling" of guest atoms. To demonstrate that "rattling" represents the major origin of phonon scattering, a triple axis neutron spectroscopy study has been recently performed which probed the coupling of vibrations of guest atoms and the surrounding framework.[40]

$Yb_{14}AlSb_{11}$

High temperature thermoelectric applications have been dominated by Si-Ge alloys because of the limited thermal stability of most intermetallic thermoelectrics. $Yb_{14}AlSb_{11}$ provides an alternative choice.[41] $Yb_{14}AlSb_{11}$ adopts the structure of $Ca_{14}AlSb_{11}$. The formula unit is composed of one $[AlSb_4]^{9-}$ and one $[Sb_3]^{7-}$ polyanion as well as four Sb^{3-} anions and $14Yb^{2+}$ cations. The identification of polyanions and assignment of charges follows from the Zintl concept. The balanced charge results in an intrinsic characteristic with a poor carrier concentration. Similar to other intrinsic semiconductors, extrinsic properties can be pronounced by rational chemical doping. In this case, hole injection was achieved by the substitution of Mn^{2+} for Al^{3+}. A complete examination of $Yb_{14}Mn_xAl_{1-x}Sb_{11}$ identified that a peak of *ZT* of 1.1 occurs at 1200 K when x reaches 0.4.[42] The existence of two cation species can be used to tune the carrier concentration. La^{3+} substitution for Yb^{2+} can back fill one electron

to the valence states.[43] The low thermal conductivity of $Yb_{14}Mn_xAl_{1-x}Sb_{11}$ may be explained by defects and disordering introduced by chemical alloying and a large unit cell structure.[2,19]

Zn_4Sb_3

Outstanding thermoelectric properties have been reported for β-Zn_4Sb_3 which is the room temperature modification of Zn_4Sb_3.[44,45,4,46,47,48,49] It was found that *ZT* values of this p-type material exceed 1 above 500 K and increase to almost 1.4 at 670 K (cf. figure 1.5). Zn_4Sb_3 has an ideal temperature range for automotive waste heat recovery. The key to the high thermoelectric performance of β-Zn_4Sb_3 lies in the exceptional thermal conductivity, which is even lower than that for clathrates.[50,51]

The origin of the remarkably low thermal conductivity of β-Zn_4Sb_3 remained a mystery until very recently when Snyder et al. reported an unusual and intricate form of disorder in this compound.[4] The disorder is expressed as a combination of Zn defects in a regular framework with composition Zn_6Sb_5 and Zn interstitials. The ideal composition of Zn_4Sb_3 was found to be $Zn_{13}Sb_{10}$ which corresponds to an electron precise situation of a narrow gap semiconductor with a completely filled valence band (see below). The actual composition, however, is $Zn_{13-\delta}Sb_{10}$ ($\delta = 0.2 – 0.5$).[45] The Zn deficiency δ is thought to correlate with the p-type behavior of Zn_4Sb_3 and should control the carrier concentration. The effects of intrinsic Zn doping have been examined by Toberer et al. via a series of samples within stable composional window for pure phases.[46]

1.4 Current Strategies in Thermoelectric Materials Research

1.4.1 Thermal conductivity engineering

The outline of some state-of-the-art thermoelectric materials in the preceding sections suggests that an important strategy to increase *ZT* is to minimize κ_L. Because κ_L is quite independent of the electron structure, efforts on impeding phonon transport usually do not lead to appreciable detriments to electron transfer. Low thermal conductivity can be expected in compounds with a large average mass of constituent atoms and/or in compounds with complex, large unit cell structures. Further κ_L can be decreased by alloying or by the presence of loosely bonded atoms (rattlers) in the crystal structure. Rattlers are believed to induce isolated vibrational modes (Einstein modes) which scatter heat carrying lattice phonons.[18] Material systems with rattlers are especially skutterudites and clathrates.

Recently, however, it has been shown that a most effective means to low values of thermal conductivity is structural disorder beyond point defects (cluster or nanocrystal inclusions) because it can provide additional scattering mechanisms that also affect mid- and long-wave-length phonons. The idea of boundary scattering is especially valid for systems with reduced dimensionality where enhancements of *ZT* have been published in one dimensional nanowires[52] or two dimensional quantum wells.[53] However, it appears to be also applicable for bulk materials. The inclusion of non-periodic nano-sized precipitates in the some tellurides such as PbTe and GeTe showed substantially decreased thermal conductivity.[54,55] In this year, Biswas et al. reported that SrTe could be

endotaxially arranged in the PbTe matrix with a concentration up to 2%.[56] With the appropriate doping with Na_2Te, the system reached a thermoelectric figure of merit of 1.7 at around 800K, which is the highest observed ZT for a bulk material.

1.4.2 Power factor, $S^2\sigma$, enhancements

Another way to maximize *ZT* lies in the increase of the power factor without drastically increasing the total thermal conductivity. However, this has proven to be very difficult because σ is related to κ_e based on the Drude's free electron gas model. This is because that electrons conduct both thermal energy and charge. Also, and most important, it is currently not understood how a material can maintain simultaneously a high thermopower S and a high electrical conductivity σ. Generally, S can be approximated by the Mott equation[57]

$$S = \frac{\pi^2}{3}\frac{k^2 T}{e}\frac{d\ln\sigma(E)}{dE}\Big|_{E=E_f} \quad (1.7)$$

where σ(E) is the electrical conductivity as a function of the Fermi energy, T is the temperature and all other letters are physical constants. If we assume that the electron scattering is independent of energy, S will be a measure of the change in the density of states above and below the Fermi level. A crude insight from the Mott equation is that S is large if there is a spike of electronic states above or below the Fermi level. Intuitively, one would expect to tailor S by changing the Fermi level, for instance, by introducing resonance states.[58]

1.5 Perspective of Thermoelectric Materials Based on Zinc Antimonides

Following the "electron-crystal, phonon-glass" paradigm the question arises where else to look for materials (or rather chemical compositions) that produce a

complex crystal structure (ensuring a low thermal conductivity) and a narrow band gap at the Fermi level (indicative of a high power factor). Here Zn_4Sb_3 represents a special case. In contrast to the other high-ZT materials, Zn_4Sb_3 is not embedded into a large family of compounds, like clathrates and skutterudites. As a matter of fact, zinc antimonides (i.e. Zn_4Sb_3, ZnSb and Zn_3Sb_2) display a unique crystal chemistry, which can not be associated with that of other materials.

The binary phase diagram of Zn-Sb is shown in figure 1.7.[42] ZnSb is a stoichiometric compound with a well studied structure (CdSb type).[59] In contrary Zn rich Zn_3Sb_2 is metastable at room temperature and appears in a low-temperature (between 682 and 728 K) and a high-temperature form (between 713 and 840 K). The structures and exact compositions of the Zn_3Sb_2 phases are not firmly established. HT-Zn_3Sb_2 adopts a complex incommensurately modulated structure where the modulation vector is coupled to a small homogeneity range $Zn_{3-x}Sb_2$ ($0.167 > x > 0$).[60] The properties of Zn_3Sb_2 phases are virtually unexplored. Also thermoelectric Zn_4Sb_3 is temperature polymorphic. The disordered room temperature form (β-Zn_4Sb_3) transforms into ordered forms (α and α') at temperatures below 255 K.[61] At temperatures above 765 K high temperature γ-Zn_4Sb_3 is stable. At even higher temperatures two more modifications are proposed (δ and δ').[62] In terms of thermoelectric properties, ZnSb displays a similar power factor compared to β-Zn_4Sb_3.

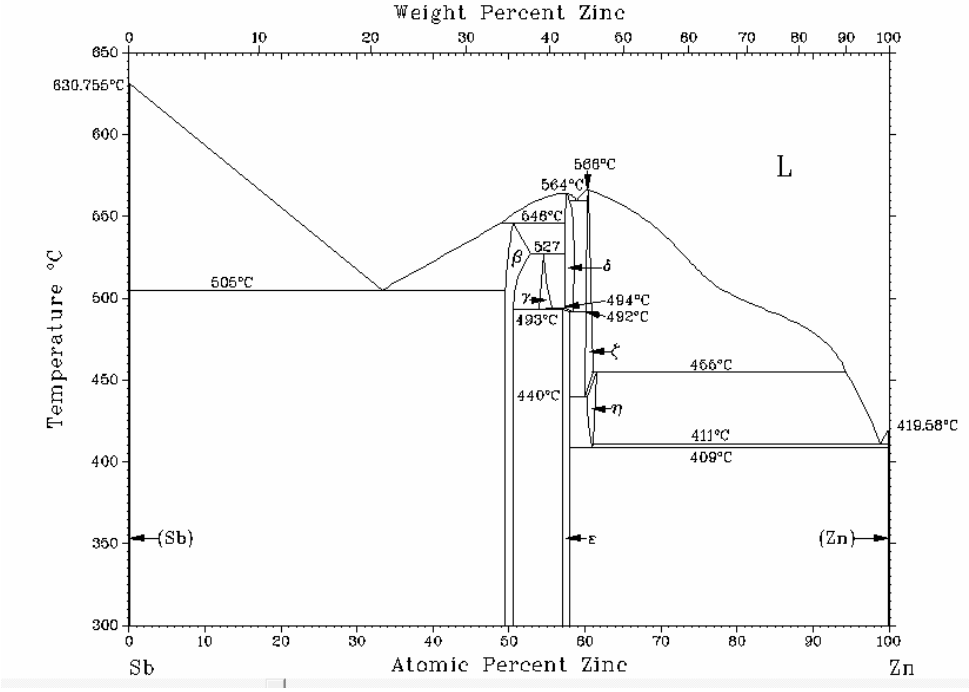

Figure 1.7. Phase diagram of Zn-Sb according to ref. 42.

The structures of zinc antimonides (if established) share a common principle, which originates in their peculiar chemical bonding. In the ZnSb structure each atom attains a five-fold coordination by one like and four unlike neighbors (cf. figure 1.8a). At the same time each atom is also part of planar rhomboid rings Zn_2Sb_2 containing a short Zn-Zn contact (2.7 Å). The arrangement of bonds and triangles (from the rhomboid ring) around each atom occurs in a tetrahedral fashion. Thus, although higher coordination numbers than four are realized, coordination is ruled by an underlying tetrahedral principle. Now one can transfer the simple bonding picture of tetrahedrally bonded III-V semiconductors to ZnSb and assign each atom in the ZnSb framework a basis set of four sp^3 hybrid orbitals.

Bonds not involved in rhomboid rings are considered as two-center two-electron (2c2e) bonds. This leaves 6 orbitals for rhomboid ring bonding. Of the resulting MOs two are bonding, and with four electrons occupying them the rhomboid ring represents a 4c4e bonded entity (figure 1.8b). Each multi-center bonded ring Zn_2Sb_2 (involving 4e) is connected with 2c2e bonds to 10 neighboring ones (involving 10e) and thus ZnSb attains an electron precise situation (electron count of 3.5 e/atom). This bonding model is in agreement with the semiconducting properties of ZnSb.

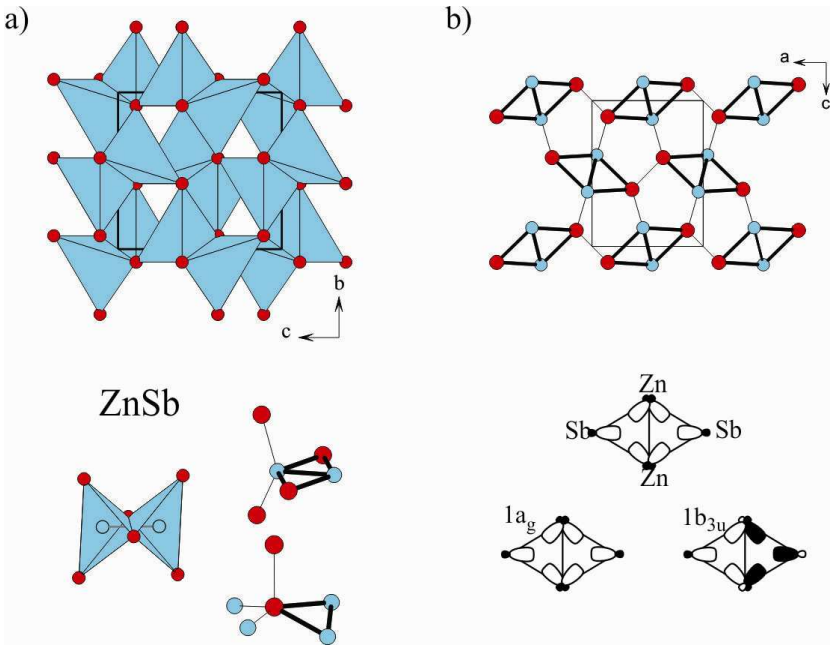

Figure 1.8. a) Top: The crystal structure of ZnSb. Bottom: Coordination of Zn (green) and Sb (red) atoms. The rhomboid ring motif is highlighted by bold bonds b) Top: Arrangement of Zn_2Sb_2 rhomboids in the ZnSb structure. Bottom: Basis set for the ring bonding and the two bonding MOs. Figures are adapted from ref. 5 & 57.

The scheme applied for ZnSb is easily extended to thermoelectric Zn_4Sb_3 (figure 1.9). The framework of the rhombohedral structure of beta-Zn_4Sb_3 (space group *R*-3*c*) consists of three atomic positions: 36 Zn, 18 Sb1 and 12 Sb2 giving a

composition Zn_6Sb_5 (figure 1.9a). Rhomboid rings Zn_2Sb_2 are condensed into chains by sharing common Sb1 atoms (figure 1.9b). These chains run in three different directions and result in a framework with channels along the *c* direction. Chains are linked to each other by 2c2e bonds and *via* tetrahedrally coordinated Sb2 atoms centering the channels. The complete Zn_6Sb_5 framework consisting of three $[Zn_2Sb1_{2/2}]$ chains and two linking Sb2 atoms is electron precise for 38 electrons. The composition Zn_6Sb_5 of the framework (37 electrons) cannot generate electron precise conditions (as shown in figure 1.9c, the Fermi level for Zn_6Sb_5 is situated in the valence band), and in thermoelectric Zn_4Sb_3 this is balanced by intricate Zn disorder, which is expressed by the occurrence of defects in the framework and interstitial Zn atoms. The actual composition of Zn_4Sb_3 – as established from the crystallographically ordered low-temperature forms - is close to $Zn_{13}Sb_{10}$ ($Zn_{6.5}Sb_5$) which corresponds to an electron precise situation.[63]

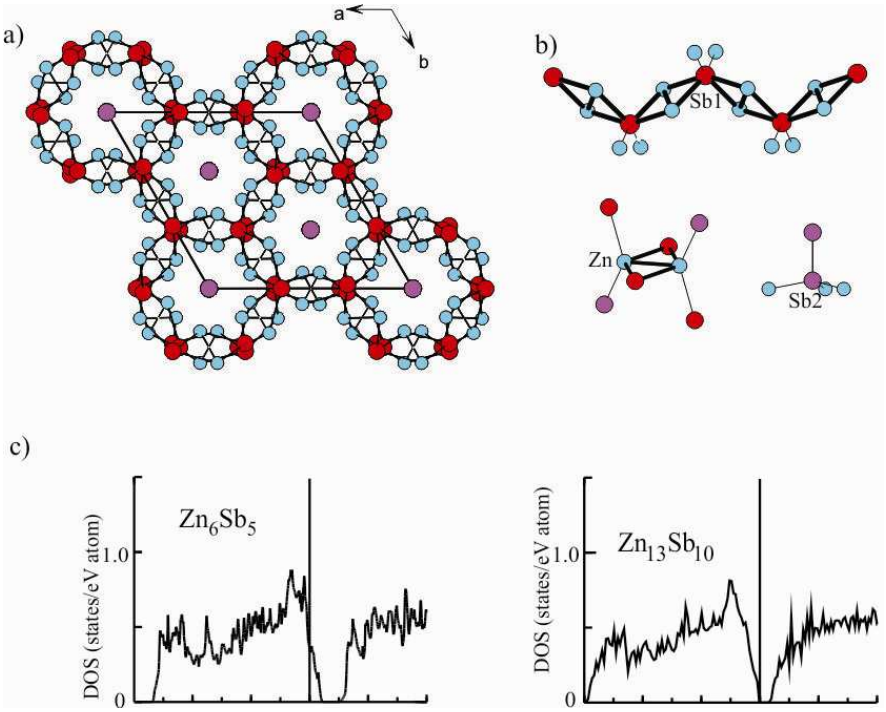

Figure 1.9. a) Framework Zn_6Sb_5 in β-Zn_4Sb_3 along [001]. Zn_2Sb_2 rhomboid rings are condensed into chains $Zn_2Sb1_{2/2}$. b) Coordination of Zn (green), Sb1 (red) and Sb2 (purple) atoms. c) DOS of Zn_6Sb_5 and $Zn_{13}Sb_{10}$ (ordered α-Zn_4Sb_3). Figures are adapted from ref. 5.

Zinc antimonides and related cadmium antimonides have been termed "electron poor framework semiconductors".[5] "Framework semiconductor" refers to a material with a structure where all constituting atoms participate in a common framework. This expresses the weakly polar character, as opposed to e.g. salt-like Zintl phases ($CaSi_2 = [Ca^{2+}][Si^-]_2$). "Electron poor" refers to a *sp* bonded framework with electron counts lower than 4 per atom, as opposed to exactly 4 in tetrahedral frameworks. The resulting multi-center bonding is thought to be a key to structural complexity. Can this concept be broadened to more materials? Can new materials be found that realize the structural and chemical bonding principles of zinc antimonides, which are obviously beneficial for thermoelectric properties?

This thesis is concerned with the search for such materials. As a strategy, the ternary system Zn-Sb-In was investigated with the goal to achieve novel ternary compounds. The choice of In was based on its electronegativity and size being similar to Zn and Sb. This was deemed necessary in order to maintain a weak polarity in the potential ternary compounds. Target compositions were aimed at electron counts lower than 4. Another aspect of this thesis was to look a little more closely at the possible reasons for "electron poor framework semiconductors" being good thermoelectrics. For example, can their multi-center bonding features induce desired resonance states in the density of states? Or, what is the origin of the low, glass-like, thermal conductivity of these materials? It appears that this feature is not restricted to classic, randomly disordered beta-Zn_4Sb_3 but a rather general phenomenon for antimony based electron poor framework materials, including ordered α-Cd_4Sb_3 and α-Zn_4Sb_3.[55,64] The elucidation is challenging but will be important for a more fundamental understanding of lattice thermal conductivity in complex intermetallics with implications to thermoelectric materials design.

Lately, $\beta-Zn_4Sb_3$ was anticipated to replace and PbTe in commercial thermoelectric applications.[65] Zinc antimonides are cheaper materials and more environmental friendly. However, samples of $\beta-Zn_4Sb_3$ display a rather low thermal stability (only up to about 673 K) and tend to lose Zn.[66] This is moderately suppressed in samples prepared by a new zone melting technique,[67] or by reducing the impurities.[68] It is interesting to see if ternary materials show higher thermal stabilities.

In particular, this dissertation addresses three major aspects.

1. The synthetic search for new "electron poor framework semiconductors" in the system Zn-Sb-In along with their phase and crystal structure characterization is presented in chapter 3. It has been shown that indium can be incorporated into Cd_4Sb_3 (which is structurally very similar to Zn_4Sb_3) by replacing cadmium.[69] Whether or not the In chemistry is similar to that in Zn_4Sb_3 is an interesting aspect.

2. A comprehensive physical property analysis for the obtained ternary Zn-In-Sb compounds is given in chapter 4. Physical property measurements included electrical and thermal conductivity, Seebeck coefficient, and carrier concentration and mobility. Further, the thermal stability of the new Zn-In-Sb was investigated and attempts were undertaken to establish structure-property correlations.

3. What makes the $\beta-Zn_4Sb_3$ stay in the pool of promising thermoelectric materials is its glass-like thermal conductivity. The general feature of electron poor antimonides having low thermal conductivities is addressed in chapter 5. First the lower limit of the thermal conductivity of Zn-Sb frameworks is established by the investigation of the amorphous alloy $Zn_{41}Sb_{59}$. Then possible mechanism behind their glass-like thermal conductivity is discussed.

Chapter 2

EXPERIMENT METHODS

Solid state chemistry involves chemical synthesis, structural characterization and physical property measurements. These three aspects are closely linked and their balance is critical for establishing the important relationships between structure and properties of a solid material. Understanding and controlling such structure-property correlations are at the heart of solid state chemistry and also the basis for developing new materials with potential technological applications.

The past decade has seen large improvements in methodologies and instrumentation concerning the synthesis of materials as well as their structure and property characterization.[70] Additionally, computational modeling of structure and phase stability, electronic structure, and physical properties has become feasible for larger (>50 atoms/unit cell) systems and provides today guidance for materials synthesis and design. These developments have very much benefited thermoelectric materials research where complex phase relations and crystal structures frequently occur. The phase and structure analysis of materials with large unit cell structures and displaying simultaneously disorder was hardly accessible in the last century.

2.1 Materials Synthesis

The two primary methods to prepare the thermoelectric materials are: 1) hot pressing and sintering and 2) crystal growth from a melt. In the first method, starting materials are compacted and annealed at high temperatures until the desired phase is formed. Mechanisms involved are diffusion, recrystallization and

grain growth.[15] In the second method, starting materials are melted and the target phase crystallizes upon cooling. The crystallization of the material is sensitive to the applied cooling condition. Direct cooling from the melt can produce polycrystalline samples with randomly oriented grains, polycrystalline samples with a preferred crystal orientation or single crystalline samples. Single crystals are critical in regards to physical property characterizations, since ambiguities due to compositional inhomogeneities, cracks and grain boundaries in the sample are avoided.

2.1.1 Crystal Growth with Molten Metal Flux

In practice the growth of crystals for solid state materials may turn out difficult. Elevated temperatures are always required since the diffusion coefficients are low. The direct combination of elements or binary compounds can be successful in providing crystals, however, there are limitations. Often these reactions are likely to produce the most thermodynamically stable compounds; the possibilities for kinetic control are relatively small. Also compounds with low(er) melting or decomposition temperatures may not be accessible from the direct combination of elements or binary precursors. In these cases molten metal fluxes have been proven to be very versatile. This type of synthesis allows the preparation of intermetallics at comparably low temperatures and yields compositionally homogenous, highly crystalline, products.[71] Because of the low synthesis temperature and/or the chemical environment provided by the surrounding molten metal, reactions are sometimes kinetically controlled. Thus,

thermodynamically weakly stable or even metastable materials can become accessible by molten metal flux synthesis.

For selecting a metal to be a viable flux medium several characteristics should be taken into account. First, the metal should possess a reasonable low melting point so that conventional containers and techniques could be used. Second, the difference between its melting point and boiling point should be large enough to ensure a stable flux medium. Third, it should not be difficult to remove the metal from the phases formed in the flux. Last but important, the metal flux should not form highly stable binary phases with any reactant.[71] Metals with low melting points, such as Pb, Sn, Ga, In, etc have been extensively researched as flux mediums to either promote crystal growth[72,73] or stabilize "kinetic" phases, such as $\beta-SiB_3$ formed in a Ga flux.[74] As a recent development, eutectic combinations of two metals have been employed as flux medium which enhances greatly the versatility of this synthesis method. For instance, the carbide Ca_2LiC_3H was obtained from a Ca/Li flux,[75] where both Ca and Li participated in the reaction. The structure of the novel carbide-hydride contains rare C_3^{4-} entities.[76]

Molten metal flux synthesis is effective for preparing binary phases in the Zn-Sb system. According to the Zn-Sb phase diagram (figure 1.7), ZnSb melts incongruently and forms a liquid and the high temperature phase of Zn_4Sb_3 at 819 K. To synthesize mm-sized crystals of ZnSb, reaction mixtures with 55 at.% Sb are slowly cooled through the liquidus, e.g. from 823 K to 793 K, and subsequently centrifuged (see below). In this case excess Sb acts as a reactive flux.

Similarly, single crystals of Zn_4Sb_3 and metastable Cd_4Sb_3 were grown by using a third metal (Bi, Sn, Pb) as a flux medium.[77,64]

2.1.2 Apparatus Setup and Crystal Growth Strategy for Compounds in the Zn-Sb-In System

Because of the positive experience with the synthesis of binary Zn-Sb and Cd-Sb compounds molten metal flux synthesis was also considered for the exploration of the ternary Zn-Sb-In system. Indium served as a reactive flux. All materials used for synthesis were prepared and handled in a dry-argon filled glove box. Pure Zn (granules, 99.99%), Sb (powder, 99.5%) and In (ingot, 99.99%) were purchased from Sigma Aldrich. Powdered Sb was pressed into a pellet. Mixtures of Zn, Sb, and In were then loaded into specially prepared silica tubes. The experimental setup is schematically depicted in figure 2.1. The silica tubes contained crushed silica which was held on the top of the tube by a quartz wool plug. After flame sealing under vacuum ($<10^{-5}$ mbar) ampoules were placed into a well insulated stainless-steel container. Reactions were carried out in a box furnace with a programmable temperature controller. Firstly, the temperature was raised to 923 K and kept for 24 h to homogenize the metal mixture. Subsequently the temperature was lowered to 598 – 748 K at rates between 2 and 5 K/h and the reaction mixture was held at this temperature for 48 h. The actual crystallization and holding temperatures depend on the composition of the reaction mixture and can be determined by a DTA analysis (cf. Appendix A.1). When the reaction was finished, the stainless steel reactor was flipped quickly and transferred into a centrifuge. The excess of flux medium is then filtrated through the quartz wool

(isothermal centrifugation). This procedure resulted in mm-sized specimens of agglomerated crystals (on top of the quartz wool filter) which were suitable for structure and property characterization.

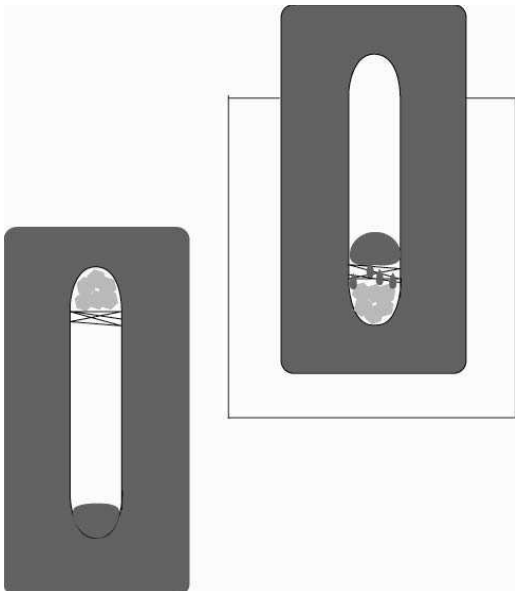

Figure 2.1. Schematic of a molten metal flux synthesis. Left, during a reaction the flux medium and reactants are at bottom. Right, after reaction, the container is quickly turned upside down and the flux medium is removed by centrifugation.

2.2 Crystal Structure Characterization and Phase Analysis

2.2.1 Single crystal data collection

Crystal structures were elucidated from single crystal X-ray diffraction. Suitable crystals were obtained by crushing a large crystal specimen obtained from the flux synthesis. Crystal quality and unit cell parameters were determined first on a Bruker AXS diffractometer at ASU, using the APEX II software for data collection and reduction.[78] Selected single crystal specimens were then sent to Stockholm University for intensity data collection. Data collection was performed at RT (295 K), 200, 150, and 120 K on an Oxford Diffraction Xcalibur 3 CCD

diffractometer with monochromatic Mo K radiation (λ = 0.71073 Å) at 50 kV and 40 mA and equipped with an Oxford cryo system cooler. The sample-to-detector distance was 50 mm. Oxford Diffraction's CrysAlis[79] software was employed for data reduction and integration.

Structures were solved by using the charge flipping algorithm as implemented in the Superflip program.[80] The charge flipping algorithm as a method of structure solution was developed by Ozlanyi and Suto.[81] It alternates between reciprocal space and real space in the manner of Fourier recycling since the relationship between the electron density and structure factors is a unitary mapping. At the beginning of the charge flipping, random phases $\varphi_{rand}(H)$ were assigned to all experimental amplitudes while making all unobserved ones equal to zero. A cycle consists of following steps.[82]

1. The electron density $\rho^{(n)}$ is derived by the inverse Fouier transformation of experimental amplitudes $F^{(n)}$.

2. A threshold δ is given. All electron densities $\rho^{(n)}$ below δ are flipped by multiplying -1 but the rest is kept the same to yield modified densities $g^{(n)}$.

3. By Fourier transformation, temporary structure factors $G^{(n)}$ are calculated from $g^{(n)}$ and the new phases $\varphi_G(H)$

4. New structure factors $F^{(n+1)}$ are obtained by combining the $\varphi_G(H)$ and the experimental amplitudes. These new structure factors are the input for the next circle of iteration. These steps will be performed iteratively until a convergence appears.

The only variable in the charge flipping algorithm is δ. The important aspect for charge flipping is that it operates without any information of symmetry. Obtained structure model were least-square refined against F^2 data using the programs JANA 2000[83] or SHELXL.[84]

Crystallographic information files (.cif) for characterized crystal structures were submitted to the Inorganic Crystal Structure Database (ICSD). Details and structural information can be obtained from the Fachinformationszentrum Karlsruhe, 76344 Eggenstein-Leopoldshafen, Germany, (fax: (49) 7247-808-666; e-mail: crysdata@fiz-karlsruhe.de) on quoting the depository numbers CSD-420363 (295 K), CSD-420364 (120K) for $Zn_5Sb_4In_{2-\delta}$ and CSD-421504 (orthorhombic), CSD-421505 (monoclinic) for $Zn_9Sb_6In_2$, respectively.

2.2.2 Phase and composition analysis for $Zn_5Sb_4In_{2-\delta}$ and $Zn_9Sb_6In_2$

For phase analysis powder X-ray diffraction (PXRD) patterns were collected on a Siemens D5000 diffractometer (Bragg-Brentano θ:θ geometry) using Cu Kα radiation (λ = 1.54059 Å). The program Powder Cell[85] was used to evaluate the diffraction pattern. Structural models employed for the phase analysis were established by single crystal diffraction with selected crystals from the synthesis. High temperature PXRD measurements were performed on a Bruker D8 diffractometer equipped with an Anton Parr XRK900 furnace.

Scanning electron microscopy (SEM) was employed to examine the surfaces of samples by back scattered electron imaging and energy dispersive spectroscopy (EDS). The SEM study was performed on an FEI XL-30 scanning electron microscope. More accurate chemical composition analysis was carried out with

electron probe micro analysis (EPMA) on a JEOL 8600 superprobe SEM operated at 15 KV and 30 nA. EPMA utilizes wavelength dispersive spectroscopy (WDS) instead of EDS. With this technique even neighboring elements in the periodic table, i.e. elements with an overlapping characteristic X-ray emission, can be analyzed accurately. Reference materials used as standards for EPMA were elemental Sb, InSb and ZnS for Sb, In and Zn, respectively. The ZAF (atomic number, adsorption and fluorescence) correction was employed for quantitative compositions determination.

2.3 Thermal Analysis for $Zn_5Sb_4In_{2-\delta}$ and $Zn_9Sb_6In_2$

2.3.1 Differential Thermal Analysis (DTA)

DTA measurements were performed on a Shimadzu DTA-50 using sealable stainless steel pans as sample containers. Typically the scanning range was from room temperature to 923 K. Heating and cooling rates were between 5-10 K/min. At the maximum temperature samples were equilibrated for 2-5 mins.

2.3.2 Differential Scanning Calorimetry (DSC)

DSC measurements were carried out on a TA Instrument 2910 calorimeter. Weighed samples (powder and crystalline) of ~20 mg were sealed in TA Tzero aluminum pans under dry argon. All experiments were performed with a helium flow of ~30 ml/min. Baselines were collected with two empty pans to determine the heat imbalance between the sample and reference pan. Temperature and heat flow were calibrated with Indium (T_m = 429.8 K, Δ_H = 28.58 J/g) and Zinc (T_m = 692.7 K). Scanning temperatures ranged from room temperature to 723 K at a

heating and cooling rate of 5 K/min. Baseline correction was made with the TA Instrument software Universal Analysis 2000.

2.4 Physical Property Measurements

2.4.1 Thermoelectric property measurements

Electrical resistivity, thermopower and thermal conductivity were performed on a Quantum Design Physical Property Measurement System (PPMS) equipped with the Thermal Transport Option (TTO). Large crystal specimens were selected and carefully shaped and polished into rectangular blocks (typically $4.5 \times 2 \times 2$ mm^3). The surface of the obtained specimen was free from any excess metal residual from the flux synthesis. For the thermal transport, two copper disks with extruded leads on each end were glued oppositely onto the specimen using a two-component silver-filled epoxy (Epo-Tek H20E), which provided contacts after curing at slightly elevated temperatures for a short time. The arrangement was then mounted on the TTO puck, which was subsequently loaded into the PPMS chamber and then evacuated ($<10^{-3}$ torr) for the measurement. The thermal transport measurements were conducted in a two-point configuration from 10 K to 350 K at a scanning rate of 0.3 K/min for all samples. At a certain temperature, a heat pulse was applied to the sample to create a temperature gradient of 3% with respect to the sample temperature. Thermal conductivity and Seebeck coefficient were obtained when the sample was equilibrated (cf. Appendix A.2). The autorange feature of the PPMS system was used in all of the measurements. Radiation heat loss was automatically corrected with the incorporated functions of the software. More accurate resistivity data were acquired with a 4-probe in-line

configuration using the resistivity option on the same PPMS, as shown in figure 2.2, by introducing a DC current of up to 1 mA. Single cooling and cooling-heating measurements from 10 K to 350 K were performed at a rate of 1 K/min, respectively.

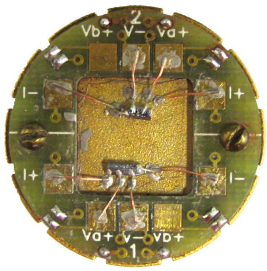

Figure 2.2. The experimental setup for a 4-probe in line arrangement for resistivity measurements on a PPMS resistivity puck.

2.4.2 Measurements of charge carrier concentrations for $Zn_5Sb_4In_{2-\delta}$

Hall measurements were carried out on a custom computer-controlled system designed in accordance with the van der Pauw configuration. The entire system composed of a 7½ Agilent 34420A voltmeter, a high impendence Keithley 7065 Hall card in a Keithley 7001 switch matrix, and a Keithley 200 current source. All devices were connected to center conductors through a triax cable, where the inner shield was guarded and the outer shield was connected to the ground.

To obtain samples suitable for the van der Pauw arrangement, finely ground powders were cold-pressed into a cylinder (4.2 mm in diameter and 8.0mm in length) in a multi-anvil device and then cut with a diamond saw with isopropanol

as cooling liquid to afford thin disks (0.5 mm in thickness). Four contacts with gold bonding wires were painted with Demetron D200 silver paint on the sample edges, which allowed resistivity and Hall measurements at the same time. The influence of the Nernst, Righi-Leduc, thermoelectric and geometric effects was eliminated by rotating the current and voltage electrodes, as well as the poles of magnetic fields were switched in the case of Hall measurements.[86] A set duration time of one second was used between the switching. The cryostat of a Quantum Design's physical property measurement system (PPMS) was employed to control the temperature from 10-350 K and to apply magnetic fields perpendicular to the sample plane at 0.4 T. The current through the samples for both Hall and resistivity measurements was typically 10 mA. The Hall coefficient can be calculated by[16]

$$R_H = -\frac{1}{ne} = \frac{V_H d}{IB} \quad (2.1)$$

where n is the carrier concentration, e is the electron charge, V_H is the Hall voltage, I is the current through the sample, B is the magnetic flux density and d is the thickness. The resistivity from van der Pauw configuration was calculated according to ref. 87.

Charge carrier concentrations were also investigated by infrared reflective spectroscopy using a Bomem DA-8 Fourier transform interferometer with a wide frequency range of 80 – 5000 cm^{-1}. In heavily doped semiconductors, charge carriers correspond approximately to that of free charges. According to the Drude

model, the oscillation of free charges with respect to the ions in the lattice can be considered as plasmas, with a characteristic frequency ω_p[88]

$$\omega_p^2 = \frac{4\pi n e^2}{\varepsilon_\infty m^*} \quad (2.2)$$

In equation 2.2 n is the carrier concentration, m^* is the effective mass and ϵ_∞ is the complex dielectric constant at infinite frequency. The dielectric constant function $\epsilon(\omega)$ is obtained by a Kramer-Kronig transformation of reflection spectra.[88] The imaginary part $\mathrm{Im}(-1/\epsilon(\omega))$ offers the information about ω_p from its peak position and scattering rates from its width.

Chapter 3

SYNTHESIS, STRUCTURES AND PHASE RELATIONS OF $ZN_5SB_4IN_{2-\delta}$ (δ = 0.15) AND $ZN_9SB_6IN_2$

3.1 Introduction

As previously described, the combination of structural complexity, weak polarity, and a narrow band gap gives zinc and cadmium antimonides interesting thermoelectric properties. The peculiar structural, bonding and electronic properties of these materials are not easily maintained in ternary systems. For example, in conjunction with electropositive metals (alkali, alkaline earth, rare earth) typically Zn/Cd and Sb atoms form commonly polyanions in now rather polar Zintl phases.[89] Reactions with indium, however, provide an interesting possibility to modify the electron poor framework structures of zinc and cadmium antimonides while maintaining a weak polarity in the ternary compounds. Recently a ternary derivative of Cd_4Sb_3, $Cd_{13-x}In_ySb_{10}$, was reported, where trivalent indium appears to replace a considerable concentration of divalent cadmium.[90] This results in a framework structure which in contrast with Cd_4Sb_3 does not contain interstitial Cd atoms.[64] In this chapter, it is shown that contrary to the Cd-Sb-In system, indium does not produce a substitutional variant of a known zinc antimonide structure, but segregates into distinct crystallographic positions in new, ternary, crystal structures.[91,92] This study centered on the zinc rich corner in the Zn-Sb-In system. All synthesis was confined to compositions containing up to 40 at. % of In and 50 at.% of Sb to avoid thermodynamically stable binaries, InSb and ZnSb.

3.2 Synthesis and Phase Analysis of $Zn_5Sb_4In_{2-\delta}$ and $Zn_9In_6In_2$

Figure 3.1 summarizes the applied reaction mixtures used and corresponding temperatures where flux conditions are maintained. (Note, that synthesis temperatures increased with increasing Sb concentrations, which were illustrated with deeper colors). Additionally the products are indicated. With respect to reaction products one can discern three regions: (1) High In concentrations yield the ternary compound $Zn_5Sb_4In_{2-\delta}$. (2) High Sb concentrations (and accompanying higher temperatures) favor the formation of Zn_4Sb_3. (3) A ternary compound with higher at. % Zn, $Zn_9Sb_6In_2$, is obtained in the intermediate region.

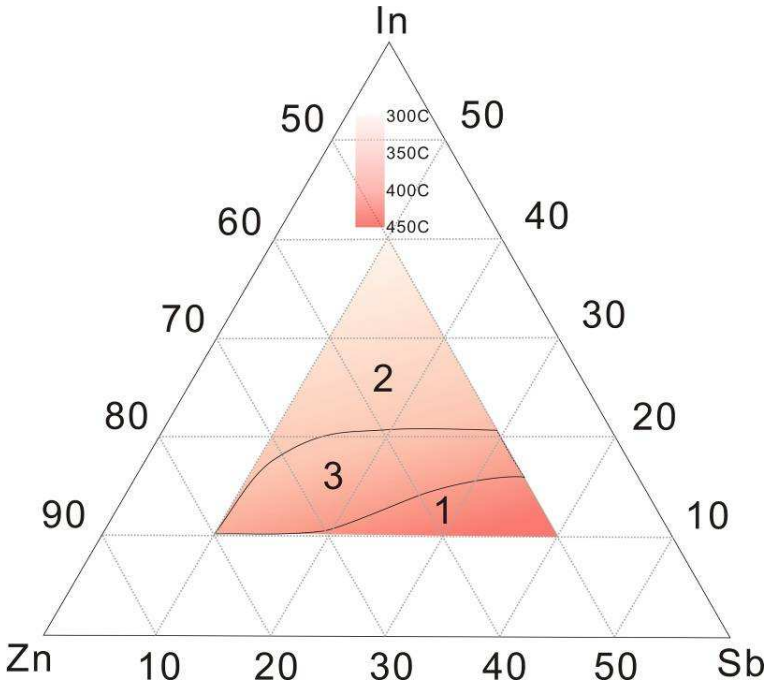

Figure 3.1. Synthesis diagram for $Zn_5Sb_4In_{2-\delta}$ and $Zn_9Sb_6In_2$. The colored triangle marks the investigated compositions. The inscribed color code indicates the flux temperatures. Product regions: **1** –Zn_4Sb_3; **2** –$Zn_5Sb_4In_{2-\delta}$ with traces of InSb; **3** – $Zn_9Sb_6In_2$ upon quenching. Compositions on axes are in at. %.

Importantly, attempts to synthesize $Zn_5Sb_4In_{2-\delta}$ from stoichiometric melts always produce a mixture of $Zn_5Sb_4In_{2-\delta}$, Zn_4Sb_3 and InSb, which indicates that the ternary compound melts incongruently. In contrast, flux synthesis with higher In (and Zn) concentrations (i.e. region (1)) yields $Zn_5Sb_4In_{2-\delta}$ virtually phase pure and in the form of mm-sized crystals. Depending on synthesis temperature and composition the product may contain traces or small amounts of InSb. Figure 3.2a shows representatively the powder pattern of the product from the synthesis mixture $Zn_{50}Sb_{20}In_{30}$ annealed at 623 K corresponding to $Zn_5Sb_4In_{2-\delta}$ as the major product.

A second ternary compound, later established as $Zn_9Sb_6In_2$, was first recognized in a reaction mixture $Zn_{62.5}Sb_{25}In_{12.5}$ annealed at 723 K, but could subsequently not be reproduced. This raised the suspicion that the compound may be metastable and decomposing if not quenched. In the routine way of finishing off reactions, crystalline products were left in the insulated stainless steel container after centrifugation to cool radiantly to room temperature (cf. experimental section). Indeed, when silica jackets were taken out of the steel container immediately after centrifugation and quenched in ice water the crystalline product corresponded reproducibly to $Zn_9Sb_6In_2$. Subsequently a larger number of reactions were repeated and finished off by this procedure, which yielded $Zn_9Sb_6In_2$, together with minor amounts of $Zn_5Sb_4In_{2-\delta}$. Figure 3.2b shows representatively the powder pattern of the product from the synthesis mixture $Zn_{60}Sb_{25}In_{15}$ annealed at 698 K and subsequently quenched. The great

similarity to the powder pattern of $Zn_5Sb_4In_{2-\delta}$ indicates a very close structural similarity.

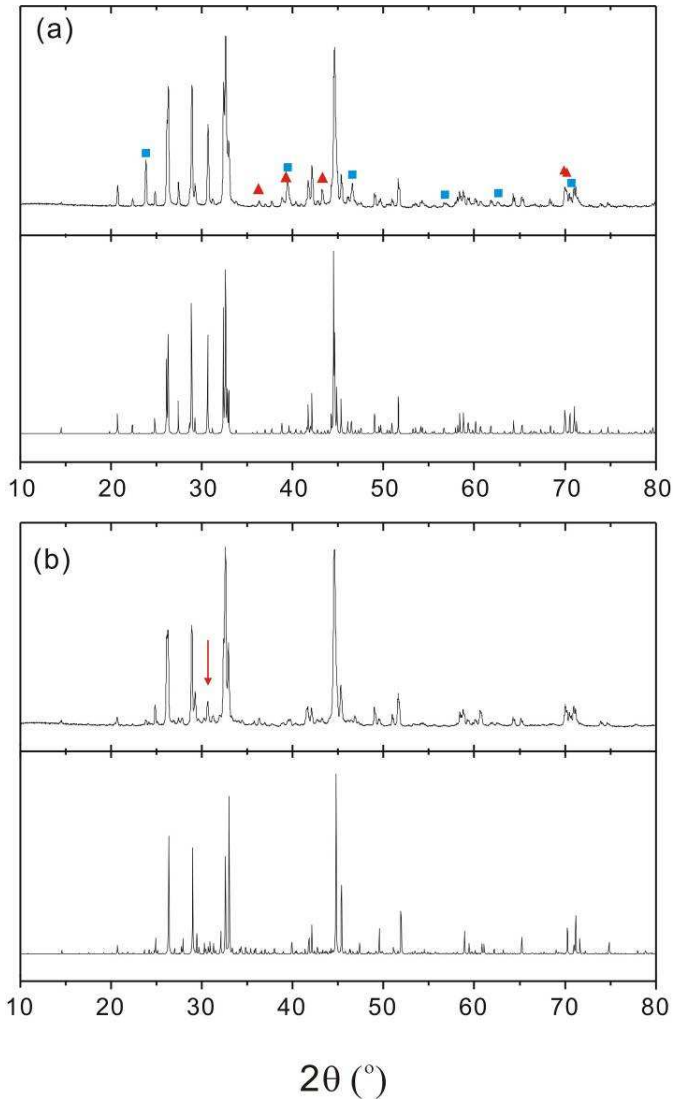

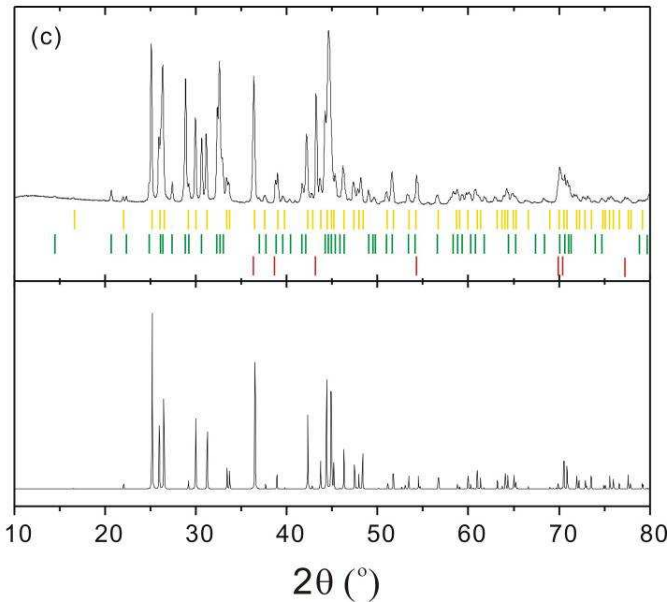

Figure 3.2. (a) Powder XRD pattern (Cu Kα) for the product of sample $Zn_{50}Sb_{20}In_{30}$ (top). Square and triangle symbols mark reflections from the byproducts InSb and Zn, respectively. The calculated pattern for $Zn_5Sb_4In_{2-\delta}$ is shown below. (b) Powder XRD patterns for the product of sample $Zn_{60}Sb_{25}In_{15}$ (top). This product represents a macroscopic mixture of $Zn_9Sb_6In_2$ and a small amount of byproduct $Zn_5Sb_4In_{2-\delta}$. The arrow marks a reflection from $Zn_5Sb_4In_{2-\delta}$. The calculated pattern for $Zn_9Sb_6In_2$ is shown below. (c) Powder XRD pattern of the product mixture obtained after annealing $Zn_9Sb_6In_2$ at 573 K (top). $Zn_9Sb_6In_2$ decomposes quantitatively into $Zn_5Sb_4In_{2-\delta}$, Zn_4Sb_3 and elemental Zn, indicated with yellow, green and red reflection markers, respectively. The calculated pattern below is for β-Zn_4Sb_3.

The metastable nature of $Zn_9Sb_6In_2$ was confirmed in DTA experiments (figure 3.3). The broad exothermic event in the trace for $Zn_9Sb_6In_2$ with a maximum around 485 K is attributed to its decomposition into the thermodynamically stable mixture. PXRD analysis of a sample $Zn_9Sb_6In_2$ annealed at 573 K for 1 h identifies the constituents of this mixture as $Zn_5Sb_4In_{2-\delta}$, Zn_4Sb_3 and elemental Zn (figure 3.2c). Thermal events at higher temperatures (above 600 K) must be inherent to this mixture. Between 570 K and 680 K, $Zn_5Sb_4In_{2-\delta}$ most likely undergoes several high temperature phase transitions,

which are not well investigated yet, and decomposes above 700K (see chapter 4.5). Events in the trace for $Zn_9Sb_6In_2$ above 700 K resemble that for pure $Zn_5Sb_4In_{2-\delta}$.

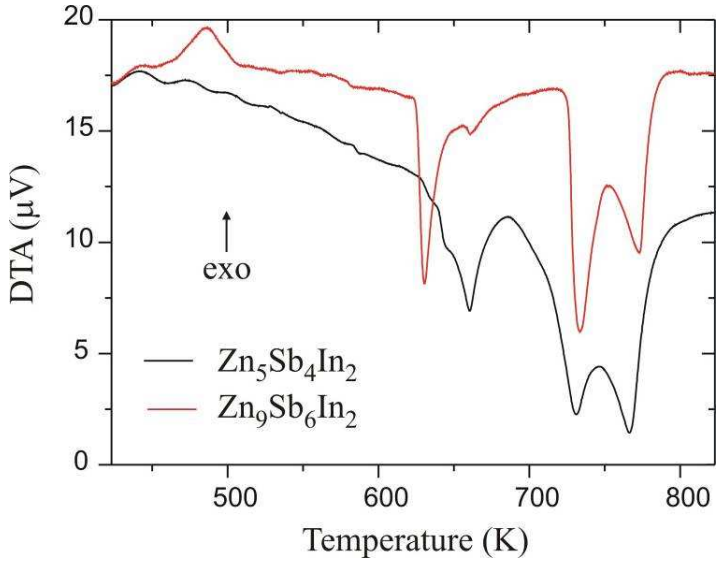

Figure 3.3. DTA heating traces for $Zn_9Sb_9In_2$ (red line) and $Zn_5Sb_4In_{2-\delta}$ (black line).

3.3 Crystal Structure Elucidation

3.3.1 Structure solution and refinement of room- and low- temperature $Zn_5Sb_4In_{2-\delta}$

The diffraction patterns for $Zn_5Sb_4In_{2-\delta}$ and $Zn_9Sb_6In_2$ can be both interpreted as orthorhombic superstructures of a tetragonal, *I*-centered, basis lattice with $a_{tet} \approx 8.7$ and $c_{tet} \approx 7.15$ Å. The patterns of the former compound can be indexed in an orthorhombic unit cell ($a \approx 7.16$ Å, $b \approx 17.15$ Å, $c \approx 8.69$ Å). The room temperature measurement shows unambiguously systematic extinctions in the Bragg reflections compatible with the space group *Pbcn*. At 120 K the **n**-glide perpendicular to *c* and the **c**-glide perpendicular to *b* are both violated by many

reflections, suggesting ordering in a subgroup to *Pbcn*. Centro-symmetric orthorhombic groups allow for two different kinds of maximal non-isomorphic subgroups, non-centric orthorhombic with the possible point group symmetries *mm*2, *m*2*m*, 2*mm* and 222 and centro-symmetric monoclinic with the point group symmetries 2/*m*11, 12/*m*1 and 112/*m* respectively. As two out of three of the glide planes are disallowed in the low temperature data, only two of these maximal subgroups is compatible with the extinction conditions, namely those with point group symmetries 222 ($P2_12_12_1$ in standard setting) and 2/*m*11, ($P2_1/c$ in standard setting). The strict adherence to the **b**-glide perpendicular to *a* (i.e. the **c**-glide perpendicular to *b* in standard setting) and the violation of the two-fold screw axis along *c* is a strong indication that the centrosymmetric monoclinic group $P2_1/c$ is the proper choice.

The structures of both the room temperature phase and the low temperature phase were solved by charge flipping, using the program Superflip.[80] The models were refined against F^2 data using the program JANA2000.[83] In the final refinements, Sb and Zn positions were considered to be fully occupied, while the occupancies of the In positions were refined. A model of the disordered room temperature phase refines to 0.053/0.138 R_1/wR_2 for all reflections. For the low temperature phase it is possible to refine an ordered, twinned, model in S.G. $P2_1/c$ to an agreement 0.042/0.121 R_1/wR_2 for *all* reflections. The applied twinning matrix (pseudo-orthorhombic cell) was (1 0 0, 0 1 0, 0 0 -1). Table 3.1 lists a summary of the refinement results.

Table 3.1. Selected Crystallographic Data for RT and LT $Zn_5Sb_4In_{2-\delta}$

Analysis for	RT	LT
formula	Zn20Sb16In7.5	Zn20Sb16In7.5
formula weight	1029.6	1029.6
crystal size, mm^3	0.049*0.063*0.089	0.049*0.063*0.089
space group	*Pbcn* (No. 60)	$P2_1/c$ (No.14)
a, Å	7.1619(2)	8.6518(2)
b, Å	17.1562(4)	7.1360(4)
c,Å	8.6887(4)	17.1158(4)
β, deg		90
Z; *V*, $Å^3$	1;1067.59(6)	1;1056.72(7)
*D*calc, gcm^{-3}	6.3783	6.475
temp, K	293K	120K
λ(Mo Kα), Å	0.71069	0.71069
absorption coeff, mm^{-1}	25.119	25.119
F(000)	1777	1784
θmin-θmax, deg	3.87-30.89	3.70-30.84
index ranges	-9≤h≤10, -24≤k≤24	-12≤h≤12, -10≤k≤9
	-12≤l≤12	-24≤l≤24
total reflns collected	15534	16233
independent reflns	1622[R(int) = 0.0328]	3067[R(int) = 0.0283]
refinement method	full-matrix least-squares on F^2	full-matrix least-squares on F^2
data/restraints/params	1622/0/59	3067/0/104
final *R* indices [$I > 3\sigma(I)$][a,b]	R_1=0.0391, WR_2=0.1267	R_1=0.0356, WR_2=0.1173
R indices (all data)[a,b]	R_1=0.0529, WR_2=0.1379	R_1=0.0416, WR_2=0.1213
largest diff. peak and hole, e^A^{-3}	2.32 and -1.62	1.81 and -1.49
GOF on F^2	1.41	1.31

[a] $R_1 = ||Fo| - |Fc||/|Fo||$. [b] $wR_2 = [w(Fo^2 - Fc^2)^2]/[w(Fo^2)^2]^{1/2}$

The chemical composition obtained from the single crystal diffraction data was confirmed by extensive electron probe micro analysis (EPMA) yielded a composition 46.8(3) at.% Zn, 35.7(3) at.% Sb, and 17.5(1) at.% In. The elemental composition of $Zn_5Sb_4In_{2-\delta}$ did not vary significantly for crystal specimens from the same sample, and between specimens from samples obtained from different

starting compositions or from applying different flux temperatures. The results from X-ray powder diffraction and electron probe microanalysis suggest that $Zn_5Sb_4In_{2-\delta}$ has no or only a very small homogeneity range.

3.3.2 Structure Solution of Orthorhombic and Monoclinic $Zn_9Sb_6In_2$

As discussed in chapter 3.3.1, the room temperature structure of $Zn_5Sb_4In_{2-\delta}$ has space group symmetry *Pbcn* with $a \approx c_{tet}$, $b \approx 2 \times a_{tet}$, $c \approx a_{tet}$. For $Zn_9Sb_6In_2$ a_{tet} appears doubled and b_{tet} trebled while c remains. The symmetry of the basic structure is *I*4*/mcm*. In orthorhombic setting this yields the full set of symmetry operations (*I* $(2,2_1)$*/(c,b)* $(2,2_1)$*/(c,a)* $(2,2_1)$*/(m,n)*). Now, doubling or trebling an axis can never convert a glide operation to a reflection (while the reverse is possible), and since there are no systematic absences for the *hk0*, *h0l* or *0kl* planes, the only possible reflection operation in the cell is the mirror plane perpendicular to z. In orthorhombic symmetry, the allowed combinations of two fold axes and reflections are limited to 2/*m* 2/*m* 2/*m*, *mm*2, *m*2*m*, 2*mm* and 222, and hence, the lone reflection perpendicular to *c* is disallowed as well. The orthorhombic space group must therefore be generated by a combination of 2 fold rotations and 2_1 screws. Inspection of the axial reflections reveals systematic absences compatible with $P2_12_12_1$ and that was the space group used to solve the structure. To phase the reflections, charge flipping was used. This yielded a set of atomic positions that quickly refined to an acceptable agreement between F^2 data and model if twinning was properly modelled. For this the program JANA2000[83] was employed. The final model treats all atomic positions with anisotropic thermal displacement parameters. In $Zn_5Sb_4In_{2-\delta}$, we detected a substantial occupational

deficiency for the In positions, and the structural model for $Zn_9Sb_6In_2$ was tested for In deficiency as well. Allowing occupational deficiency of the In positions did not result in any change of the overall composition, although two In positions became over-occupied and the other two under-occupied. The effect is slight, and the difference in fit between model and data is negligible, and consequently the structure was treated as stoichiometric with all atomic positions fully occupied. Table 3.2 lists a summary of the refinement results of orthorhombic $Zn_9Sb_6In_2$ and a monoclinic variant, which will be addressed in chapter 3.4.3.

Table 3.2 Selected crystallographic data for the orthorhombic and monoclinic form of $Zn_9Sb_6In_2$

Crystal Data	Orthorhombic	Monoclinic
formula	$Zn_9Sb_6In_2$	$Zn_9Sb_6In_{1.89}$
formula weight	1548.6	1536
space group	P 21 21 21	C11 21
a, Å	7.142(2)	17.1463
b, Å	17.146(5)	51.4388
c,Å	25.719(7)	7.1416
beta, deg		90
Z; *V*, Å^3	8, 3149.4(15)	16, 6298.785
Dcalc, gcm^{-3}	6.53	6.477
temp, K	293	293
l(Mo Kα), Å	0.71069	0.71069
absorption coeff, mm^{-1}	26.347	26.191
F(000)	5391	10696
θmin-θmax, deg	2.38-28.37	4.43-26.89
index ranges	-9⩽h⩽9, -22⩽k⩽22 -34⩽l⩽34	-18⩽h⩽21, -63⩽k⩽54 -8⩽l⩽8
total reflns collected	21287	25164
independent reflns	7183	17525
refinement method	full-matrix least-squares on F^2	full-matrix least-squares on F^2
data/restraints/params	7183/0/308	17525/0/224
final *R* indices [$I > 3\sigma(I)$]^{a,b}	R_1=0.0408, WR_2=0.0837	R_1=0.1247, WR_2=0.1341
R indices (all data)^{a,b}	R_1=0.1885, WR_2=0.1028	R_1=0.1592, WR_2=0.1379
largest diff. peak and hole, e^A^{-3}	3.21,-3.11	7.36,-5.26
GOF on F^2	1.6	4.51

$^a R_1 = ||Fo| - |Fc||/|Fo||$. $^b wR_2 = [w(Fo^2 - Fc^2)^2]/[w(Fo^2)^2]^{1/2}$

3.4 Description and Analysis of Crystal Structures

3.4.1 Room temperature $Zn_5Sb_4In_{2-\delta}$

The room temperature form of $Zn_5Sb_4In_{2-\delta}$ crystallizes with the orthorhombic space group *Pbcn* and contains 7 distinct atomic positions (Figures 3.5 and 3.6, Tables 3.1, 3.3 and 3.4). Zn1, Zn2, Sb1, and Sb2 atoms are situated on general sites 8*d*, while In1 and In2 atoms occupy sites 4*c*. The In positions display some occupational deficiency (5 – 10%) which is indicated as δ in the compound formula. The Zn3 position represents a split position (i.e. a half occupied general position 8*d*). The refined composition of $Zn_5Sb_4In_{2-\delta}$ is $Zn_5Sb_4In_{1.85(3)}$ ($\delta = 0.15(3)$).

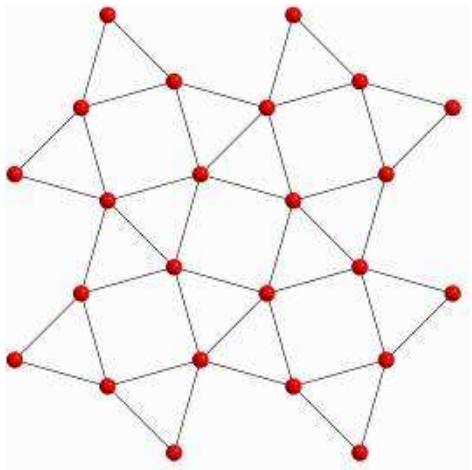

Figure 3.4. The 3^2434 Sb net.

The characteristic feature of the $Zn_5Sb_4In_{2-\delta}$ structure is 3^2434 nets (cf. figure 3.4) formed by the Sb atoms that are stacked in antiposition orientation along the *a* direction. This yields rows of face-sharing square antiprisms that are

connected in the bc plane by sharing triangle edges. Such an arrangement of 3^2434 nets occurs in many intermetallic compounds, and the most prominent is probably the $CuAl_2$ type where nets are formed by Al atoms while Cu atoms center square antiprisms. The arrangement of Sb atoms is body centered tetragonal (its unit cell is indicated in figure 3.5a) and contains also intervening tetracapped tetrahedra usually termed as tetraedersterns (figure 3.5b).[93] In some stuffed variants of the $CuAl_2$ type the center of the central tetrahedron is occupied which retains the tetragonal symmetry (e.g. in "TlSe" larger Tl^+ and smaller Tl^{3+} occupy square antiprisms and central tetrahedra, respectively).

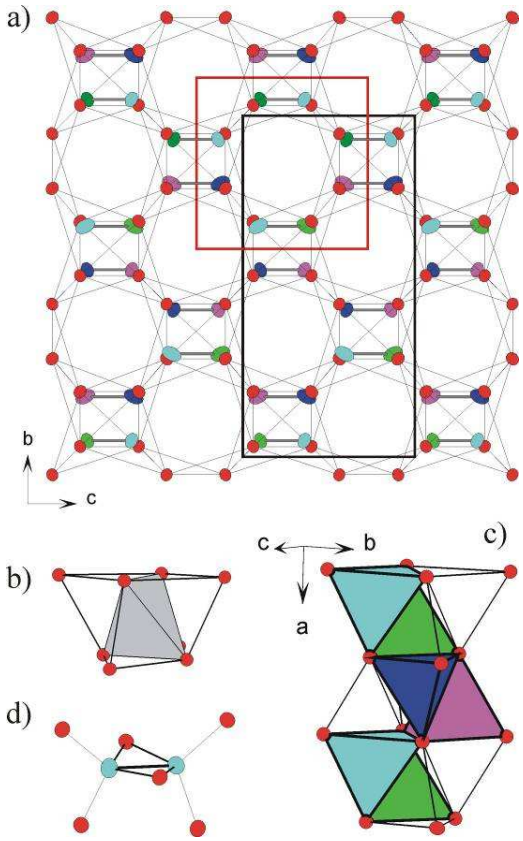

Figure 3.5. The framework "ZnSb" in $Zn_5Sb_4In_{2-\delta}$. (a) Sb atoms (red circles) form 3^2434 nets (thin lines) stacked in antiposition along the *a* direction. The unit cell of the Sb atom arrangement is outlined in red, the one of the $Zn_5Sb_4In_{2-\delta}$ structure in black. (b) Tetracapped tetrahedron ("tetraedersterns") formed by 8 Sb atoms. The central tetrahedron (empty) is marked in grey. (c) Arrangement of tetraedersterns in $Zn_5Sb_4In_{2-\delta}$ with peripheral tetrahedra occupied by Zn atoms. Different colors indicate different heights in the *a* direction (cf. (a) where pairs of Zn atoms are connected by grey, thick, lines). Cyan $x \approx 0.12$; Green $x \approx 0.38$; Blue $x \approx 0.62$; Purple $x \approx 0.88$. (d) Coordination environment of Zn atoms. Rhomboid rings Zn_2Sb_2 are emphasized with bold lines. Ellipsoids are drawn at a 90% probability.

In $Zn_5Sb_4In_{2-\delta}$, however, Zn1 and Zn2 occupy two of the four peripheral tetrahedra in Sb8 tetraedersterns while the central tetrahedron always remains empty. Those edge-shared peripheral tetrahedra result in rather short distances Zn1-Zn1 and Zn2-Zn2 (below 3 Å). The distribution of Zn atoms (or "Zn pairs")

is shown in figure 3.5c with three tetraedersterns that are consecutively stacked along the *a* direction and in figure 3.5a where different colors denote different heights along *a*. It results in a symmetry lowering of the originally tetragonal arrangement of Sb atoms to orthorhombic, and a doubling of unit cell. It should be noted that the kind of distribution of Zn atoms in tetraedersterns is unusual when considering the structure of $Zn_5Sb_4In_{2-\delta}$ as a derivative of the $CuAl_2$ type. None of the ubiquitous structures based on antiposition stackings of 3^2434 nets and different fillings in square antiprisms and tetrahedra display this kind of distribution.[94] However, the Zn distribution yields a structural fragment characteristic for binary zinc antimonides, namely rhomboid rings Zn_2Sb_2 as a part of face sharing tetrahedra $ZnSb_4$.[63] As in binary zinc antominides, Zn atoms in $Zn_5Sb_4In_{2-\delta}$ (Zn1 and Zn2) display a peculiar 5-coordination by one like atom and 4 Sb atoms (figure 3.5d).

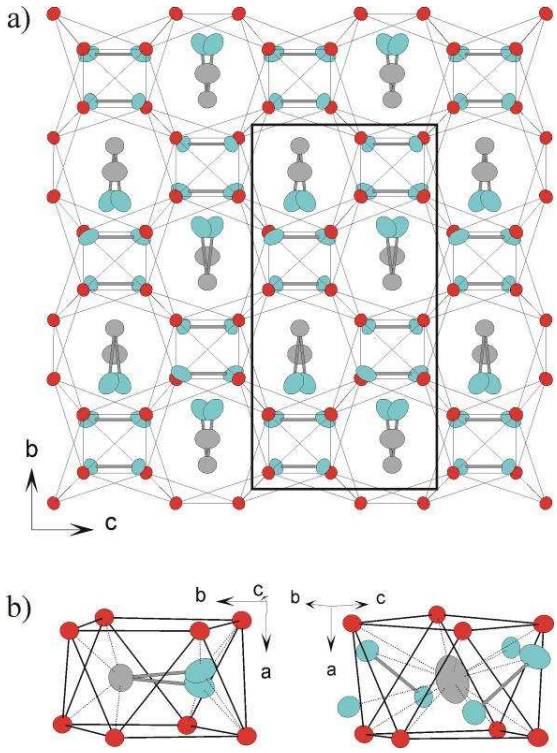

Figure 3.6. (a) The total structure of $Zn_5Sb_4In_{2-\delta}$ projected along the *a* direction. Cyan, red and grey ellipsoids denote Zn, Sb, and In atoms, respectively. Atom pairs Zn-Zn and Zn-In are connected by grey, thick, lines. (b) Coordination environment (broken lines) of atoms centering Sb_8 square antiprisms (solid lines). Left: Zn3-In1 pair, right: In1 atom. Ellipsoids are drawn at a 90% probability.

The framework of Sb and Zn1 and Zn2 atoms represents a (2 × 1 × 1) superstructure with respect to the tetragonal basis structure of Sb atoms. It has a composition ZnSb and involves 16 atoms in the unit cell. The remaining atoms (In1, In2, and Zn3) are located in the channels provided by the rows of square antiprisms (figure 3.6a). The stuffing of those channels in RT-$Zn_5Sb_4In_{2-\delta}$ does not result in any further symmetry lowering. Centers of square antiprisms are occupied alternately by pairs of Zn3 and In1 atoms, and single In2 atoms. Their coordination is shown in figure 3.6b. The distance between pairs of Zn3 and In1 atoms is peculiarly short, 2.62 Å. In2 atoms have large and anisotropic

displacement parameters (cf. table 3.3) and appear loosely coordinated by the 8 Sb atoms forming the square antiprism and additionally 6 Zn atoms. Furthermore the two pairs Zn3-In1 located in neighboring square antiprisms can also be considered coordinating In2 (not shown in figure 3.6b). The nearest neighbor distances vary continuously from 3.40 to 3.85 Å. The smallest distance is to Zn2 atoms. The Zn3 split position and the occupational deficiency of In atoms indicate disorder within the tetragonal channels formed by the square antiprisms. Also, the composition from the microprobe analysis (46.3% Zn; 35.7% Sb; 17.5% In) suggests a slightly higher Zn/Sb ratio compared to the crystallographically refined one (45.9% Zn; 36.7% Sb; 17.3% In). The redistribution of Zn atoms to the surface, which will be discussed in later chapters, could be a possible reason.

Table 3.3. Atomic coordinates and isotropic displacement parameters for room (RT) and low temperature (LT) $Zn_5Sb_4In_{2-\delta}$.

	Atom	Wyck.	Occ.	X	Y	z	U_{iso} (Å^2)
RT	Zn1	8d	1	0.6134(1)	0.55866(6)	0.3776(1)	0.0207(3)
	Zn2	8d	1	0.6202(2)	0.18741(7)	0.1102(2)	0.0286(3)
	Zn3	8d	0.5	0.0377(4)	0.7141(2)	0.7820(4)	0.042(1)
	Sb1	8d	1	0.76445(7)	0.45854(3)	0.58049(6)	0.0142(2)
	Sb2	8d	1	0.74447(7)	0.29790(3)	0.91934(7)	0.0160(2)
	In1	4c	0.891(5)	0	0.56332(7)	0.75	0.0303(4)
	In2	4c	0.952(6)	0.5	0.36577(9)	0.25	0.0623(7)
LT	Zn1a	4e	1	0.8743(2)	0.3878(2)	0.55715(8)	0.0066(3)
	Zn1b	4e	1	0.6208(2)	0.6137(2)	0.55944(8)	0.0071(4)
	Zn2a	4e	1	0.8995(2)	0.8907(2)	0.68596(9)	0.0113(4)
	Zn2b	4e	1	0.3849(2)	0.6255(2)	0.81217(8)	0.0076(3)
	Zn3	4e	1	0.7055(2)	0.4498(2)	0.78468(9)	0.0179(4)
	Sb1a	4e	1	0.91867(9)	0.76582(9)	0.54075(5)	0.0046(2)
	Sb1b	4e	1	0.57851(9)	0.23652(9)	0.54207(5)	0.0046(2)
	Sb2a	4e	1	0.9207(1)	0.26164(9)	0.70132(5)	0.0058(2)
	Sb2b	4e	1	0.5864(1)	0.74664(9)	0.70320(5)	0.0052(2)
	In1	4e	0.919(4)	0.7552(1)	0.4932(1)	0.93596(5)	0.0105(2)
	In2	4e	0.960(6)	0.7462(2)	0.9783(3)	0.86476(5)	0.0246(3)

3.4.2 Low temperature $Zn_5Sb_4In_{2-\delta}$.

At low temperatures (below 200 K) $Zn_5Sb_4In_{2-\delta}$ undergoes a structural phase transition. Additional reflections appear that violate the extinction conditions imposed by the **n**- and **c**-glide planes in *Pbcn* (figure 3.7 (a)). The symmetry is lowered to monoclinic without any change in the unit cell. In space group $P2_1/c$ the split position resolves into a single four-fold Zn position (Zn3). As a consequence, pairs Zn-In within tetragonal channels that were previously arranged parallel to the orthorhombic *b* axis are now slightly tilted with respect to this axis (the monoclinic *c* axis). This is shown in figure 3.7b. Apart from that, the structure remains virtually unchanged.

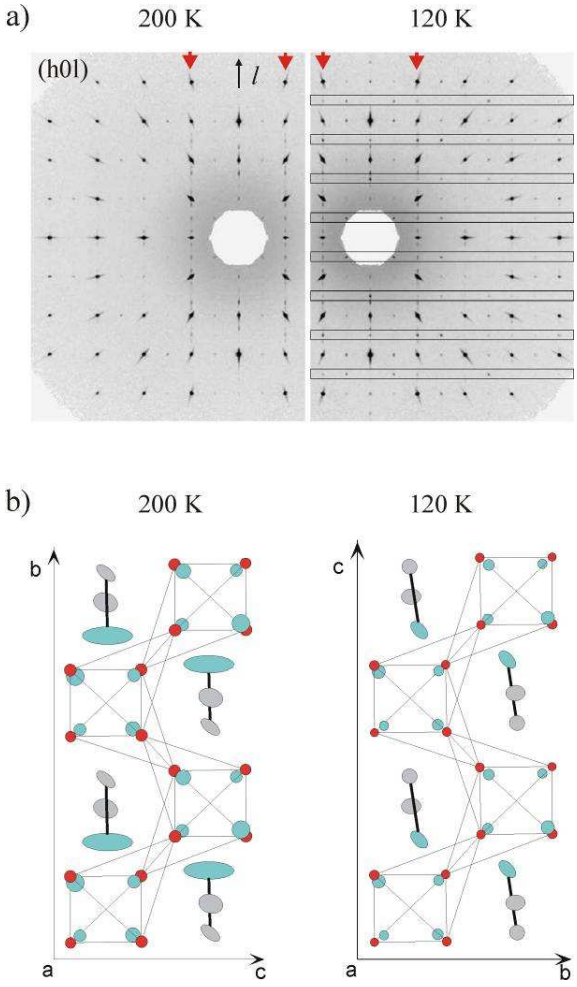

Figure 3.7. (a) Diffraction pattern of the (*h0l*) plane for $Zn_5Sb_4In_{2-\delta}$. Left: 200 K – orthorhombic room temperature form. Right: 120 K – monoclinic low temperature form. The rectangles mark the areas for odd *l* where reflections appear that violate the reflection condition for the c-glide (*h0l* : *l* = 2n) present in the room-temperature form. Red arrow heads mark rows with diffuse and additional reflections attributed to intergrown domains of $Zn_9Sb_6In_2$. (b) The crystal structure of $Zn_5Sb_4In_{2-\delta}$ at 200 K (left) and at 120 K (right). For better comparability the room temperature structure was also refined in the monoclinic symmetry of the low-temperature form. The Zn3 split position in the room-temperature form (cf. figure 3.6a) is now expressed as a single, elongated atom. Ellipsoids are drawn at a 90% probability (cyan, red and grey denote Zn, Sb, and In atoms, respectively)

The structural behavior of $Zn_5Sb_4In_{2-\delta}$ is reminiscent of binary Zn_4Sb_3. Here the room temperature phase (β-Zn_4Sb_3; S.G. *R*-3*m*) is substantially disordered which is manifested in interstitial Zn atoms distributed on three weakly occupied (to about 5%) general sites 36*f*. Upon cooling Zn_4Sb_3 undergoes two phase transitions to the consecutively higher ordered phases α and α' where interstitial Zn atoms occupy distinct crystallographic sites in highly complex low-symmetry crystal structures. One could suspect that the deviation between microprobe determined and crystallographic composition is caused by a small concentration of interstitial Zn atoms in $Zn_5Sb_4In_{2-\delta}$. When increasing the unit cell content from 20 to 21 Zn atoms (i.e. by 5%) a good agreement is obtained. However, we did not find any clear evidence for weakly occupied Zn positions in our refinements. Instead, we propose that crystals of $Zn_5Sb_4In_{2-\delta}$ contain domains of the phase $Zn_9Sn_6In_2$, which has a higher Zn content. The crystal structures of $Zn_9Sb_6In_2$ (explained below) and $Zn_5Sb_4In_{2-\delta}$ have identical ZnSb frameworks but differ in the stuffing of the tetragonal channels. Indeed, a multiphase refinement including the second phase, $Zn_9Sb_6In_2$, did yield a better fit to the data. This strategy leads to an improvement of R_1/wR_2 to 3.34/6.59 for *all* reflections, at a minority component content of 8% (120 K data).

3.4.3 Orthorhombic and monoclinic $Zn_9Sn_6In_2$

Structurally, $Zn_9Sb_6In_2$ turns out to be quite challenging. As for the previously reported $Zn_5Sb_4In_{2-\delta}$ there is a basic tetragonal pattern (figure 3.8 a) arising from the Sb substructure (*I*4/*mcm*). In $Zn_5Sb_4In_{2-\delta}$ the systematic

extinction associated with the *I*-centering is broken, and additionally both the *a* and the *b* directions exhibit satellite reflections that indicate a doubling of the corresponding axes. There is however a conspicuous lack of reflections that double the tetragonal a and b axes simultaneously, and this led us to conclude that the doubling only applies to one direction, while the second set of satellites are generated by pseudo merohedral twinning. According to chapter 3.4.1, the space group symmetry of $Zn_5Sb_4In_{2-\delta}$ is *Pbcn* with $a \approx 7.15$ Å (ctet), $b \approx 17.15$ Å ($2 \times$ atet), $c \approx 8.7$ Å (atet).

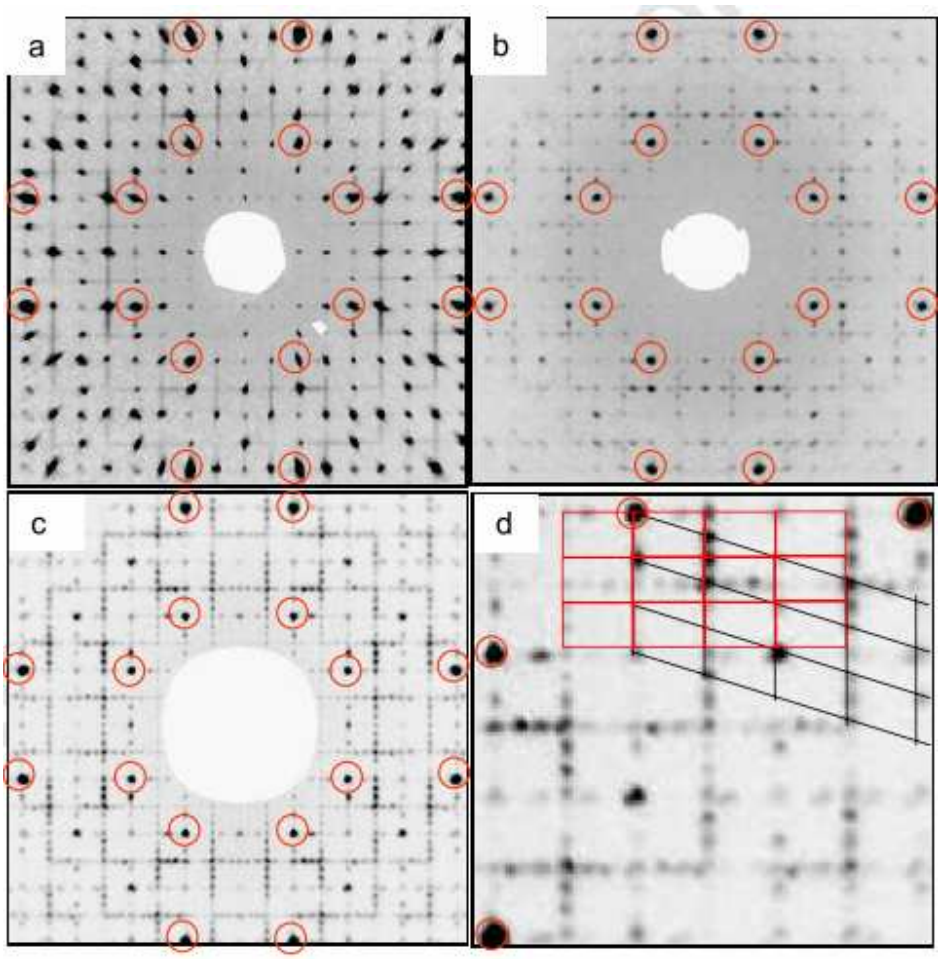

Figure 3.8. Diffraction patterns corresponding to *hkl* of (a) orthorhombic $Zn_5Sb_4In_{2-\delta}$ (b) orthorhombic $Zn_9Sb_6In_2$ and (c) monoclinic $Zn_9Sb_6In_2$. The reflections corresponding to the basic tetragonal lattice are highlighted. The diffraction pattern shown in (d) represents an enlargement of (c) where the reciprocal unit cells of orthorhombic and monoclinic $Zn_9Sb_6In_2$ have been highlighted.

The diffraction pattern of $Zn_9Sb_6In_2$ is more complex, and a cursory inspection indicates a tetragonal unit cell with a six-fold superstructure along the *a* and *b* directions (figure 3.8b). A very large number of reflections are however systematically absent, indicating twinning. With few exceptions the non-crystallographic absences are in agreement with a model where atet is doubled and btet is trebled, and where pseudo merohedral twinning generates the rest of

the reflections observed. The violations of this simple model are a weak set of reflections that double atet and btet simultaneously, and those reflections will be dealt with separately at a later stage. $Zn_9Sb_6In_2$ was assigned space group symmetry $P2_12_12_1$.

A large number of crystals were studied, and in many samples the fit between data and model was quite poor, but improved substantially when $Zn_5Sb_4In_{2-\delta}$ was introduced into the refinement as a second phase. It appears that substantial fractions of $Zn_5Sb_4In_{2-\delta}$ intergrow regularly in metastable $Zn_9Sb_6In_2$. The vice versa situation is observed as well (described in chapter 3.4.2). However, volume fractions of $Zn_9Sb_6In_2$ in crystals of $Zn_5Sb_4In_{2-\delta}$ are significantly small (up to 8%).

One particular crystal showed a distinctly different diffraction pattern. The six-fold super-structuring is much more pronounced than in $Zn_9Sb_6In_2$ and interestingly, this effect is exhibited only in every second row of reflections (figure 3.8c). The obvious interpretation is a further doubling of the long axis in $Zn_9Sb_6In_2$ but this approach proved unsuccessful in providing a structural solution. After abandoning this first interpretation, it was realized that the diffraction pattern may be generated by a two-phase crystal, where one phase is orthorhombic $Zn_9Sb_6In_2$ and the other is a monoclinic variant that generates a new set of reflections along the long axis that neatly interdigitates the reflections from the former (figure 3.8d). The symmetry of this new monoclinic phase was assumed to be $P112_1$, and the structure was solved by charge-flipping. It comes out as a simple variation of the orthorhombic form. The structure of the monoclinic form may be generated by a simple shift of a unit cell sized block of

the orthorhombic phase by the vector (½½0). To facilitate the simultaneous treatment of the two structures, the shift vector (½½0) was employed as a centering vector in the monoclinic structure. This allows a description in a metrically orthorhombic cell, twice the size of the cell of the orthorhombic phase (doubling the long b axis). Thus, both structures are described in a metrically orthorhombic cell measuring 17.14 by 51.44 by 7.14 Å. In addition to the biphasic nature of the crystal, both phases are twinned by pseudo merohedry because of the underlying tetragonal symmetry. The final agreement between the model and data is modest (R_1 is ca. 12%, cf. Table 3.2), but considering the complexity of the sample this is not unexpected.

The most prominent satellite reflections of the monoclinic phase are those that simultaneously double the *a* and *b* axes of the basic tetragonal cell. It is interesting to note that these reflections are absent both in $Zn_5Sb_4In_{2-\delta}$ and in orthorhombic $Zn_9Sb_6In_2$. These are the unexplained weak reflections present in the diffraction pattern of $Zn_9Sb_6In_2$ referred to earlier. It would seem that metastable $Zn_9Sb_6In_2$ occurs in different structural variations depending on melt composition and the thermal history of sample preparation. The same holds for the intergrowth with $Zn_5Sb_4In_{2-\delta}$. Finally, it should be mentioned that we also identified crystals were $Zn_9Sb_6In_2$ appears to be epitaxially intergrown with the binary phase Zn_4Sb_3. This shows the complexity of phase relations in the compositional region (2), even nominal “single” crystals may consist of several phases.

3.5 Structure and Phase Relationship of $Zn_5Sb_4In_{2-\delta}$ and $Zn_9Sb_6In_2$

In the following we will establish the crystal structure relationships between orthorhombic $Zn_5Sb_4In_{2-\delta}$ and $Zn_9Sb_6In_2$ (figures 3.9 and 3.10). The characteristic features of both structures are 3^2434 nets formed by the Sb atoms that are stacked in antiposition orientation (figure 3.9a). This arrangement yields rows of face-sharing square antiprisms that are connected in the tetragonal plane by sharing triangle edges. In addition to square antiprisms the Sb atom substructure generates also intervening tetracapped tetrahedra usually termed tetraedersterns (figure 3.9b).[93]

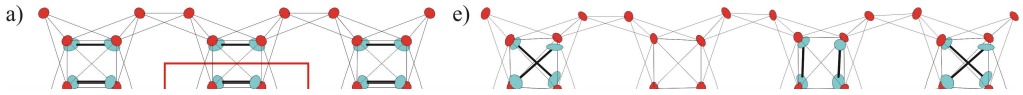
a)
e)

ERROR: ioerror
OFFENDING COMMAND: image

STACK: